FASH and MASH: *F*emale and *M*ale *A*dult human phantoms based on polygon me*SH* surfaces
Part II: Dosimetric calculations

R Kramer[1], V F Cassola[1], H J Khoury[1], J W Vieira[2,3],V J de Melo Lima[4] and K Robson Brown[5]

[1] Department of Nuclear Energy, Federal University of Pernambuco, Avenida Prof. Luiz Freire, 1000, CEP 50740-540, Recife, Brazil

[2] Federal Institute of Education, Science and Technology of Pernambuco, Recife, Brazil

[3] Polytechnic School of Pernambuco, University of Pernambuco, Recife, Brazil

[4] Department of Anatomy, Federal University of Pernambuco, Recife, Brazil

[5] Imaging Laboratory, Department of Archaeology and Anthropology, University of Bristol, Bristol, UK

Statement of provenance:
'This is an author-created, un-copyedited version of an article accepted for publication in Physics in Medicine and Biology. IOP Publishing Ltd is not responsible for any errors or omissions in this version of the manuscript or any version derived from it. The definitive publisher authenticated version is available at doi:10.1088/0031-9155/55/1/010.'

Abstract

Female and male adult human phantoms, called FASH (*F*emale *A*dult me*SH*) and MASH (*M*ale *A*dult me*SH*), have been developed in the first part of this study using 3D animation software and anatomical atlases to replace the image-based FAX06 and the MAX06 voxel phantoms. 3D modelling methods allow for phantom development independent from medical images of patients, volunteers or cadavers. The second part of this study investigates the dosimetric implications for organ and tissue equivalent doses due to the anatomical differences between the new and the old phantoms. These differences are mainly caused by the supine position of human bodies during scanning in order to acquire digital images for voxel phantom development. Compared to an upright standing person, in image-based voxel phantoms organs are often coronally shifted towards the head and sometimes the sagittal diameter of the trunk is reduced by a gravitational change of the fat distribution. In addition, volumes of adipose and muscle tissue shielding internal organs are sometimes too small, because adaptation of organ volumes to ICRP-based organ masses often occurs at the expense of general soft tissues, such as adipose, muscle or unspecified soft tissue. These effects have dosimetric consequences, especially for partial body exposure, such as in X-ray diagnosis, but also for whole body external exposure and for internal exposure. Using the EGSnrc Monte Carlo code, internal and external exposure to photons and electrons has been simulated with both pairs of phantoms. The results show differences between organ and tissue equivalent doses for the upright standing FASH/MASH and the image-based supine FAX06/MAX06 phantoms of up to 80% for external exposure and up to 100% for internal exposure. Similar differences were found for external exposure between FASH /MASH and REGINA/REX, the reference voxel phantoms of the International Commission on Radiological Protection. Comparison of effective doses for external photon exposure showed good agreement between FASH/MASH and REGINA/REX, but large differences between FASH/MASH and the mesh-based RPI_AM and the RPI_AF phantoms, developed at the Rensselaer Polytechnic Institute (RPI).

1. Introduction

Computational phantom dosimetry began almost 60 years ago with a paper by W.S. Snyder (1950) reporting neutron Monte Carlo calculations in a homogeneous, semi-infinite 30cm slab phantom representing the human trunk. Since then, numerous radiation transport calculations have been published, using various types of Monte Carlo codes for all kinds of particles, simulating many different internal and external exposure scenarios and applying a variety of computational human phantoms. From the early mathematical or stylized phantoms (Snyder et al 1978, Cristy 1980, Kramer et al 1982), over the image-based or voxel phantoms (Zankl and Wittmann 2001, Xu et al 2000, Kramer et al 2006a) to the hybrid phantoms (Lee et al 2007, Xu et al 2007) based on 3D modelling software, this development was aimed at improving the anatomical representation of the human body with every new type of phantom. For a complete overview on human phantom development the reader is kindly asked to consult reviews such as the Handbook of Anatomical Models for Radiation Dosimetry (Xu and Eckerman 2009).

For the time being, models designed by computer graphic software using polygon mesh surfaces, independent from digital images of persons, represent the latest step in human phantom development. Santos and Frère (2007a, b) constructed a mesh-based adult male phantom using box modelling of primitives with Blender (2009) based on photographic images of a skeleton and on anatomical atlases. Xu et al (2008), Zhang et al (2008a, b) and Na et al (2008) used surface mesh models for organs downloaded from the internet to develop human phantoms, which eventually led to the publication of the ICRP89-based male RPI_AM and female RPI_AF phantoms (Zhang et al 2009). Zhang et al's study includes also conversion coefficients for external exposure to photons. Having been developed independently from medical images, these mesh-based phantoms represent individuals with organ positions for standing posture.

Using MakeHuman (2009), Blender (2009), Binvox (Min 2009), ImageJ (2009), surface mesh organ models, primitive 3D surfaces and anatomical atlases, Cassola et al (2009) have developed two adult human phantoms, called FASH (*F*emale *A*dult me*SH*) and MASH (*M*ale *A*dult me*SH*), based on average organ and tissue masses according to ICRP89 (ICRP 2002).

Whatever the level of anatomical realism of the phantom applied, in radiation protection the results of dosimetric calculations are usually expressed as conversion coefficients (CCs), i.e. as ratios between quantities of interest (such as organ and tissue equivalent dose, effective dose, etc.), and measurable quantities (such as air kerma, kerma-area product, etc.), in order to be useful for the assessment of organ and tissue equivalent doses. Among other things, CCs for radiation protection can be found in reports of the International Commission on Radiological Protection (ICRP) (ICRP 1979,1996) or of the International Commission on Radiation Units and Measurements (ICRU) (ICRU 1998), which are still based on mathematical phantoms. Although the report on the ICRP reference voxel phantoms REX and REGINA is still in press (ICRP 2009), CCs for the two phantoms have already been published for external exposure to photons (Schlattl et al 2007).

2. The purpose of this study

The introduction of the two adult human phantoms FASH and MASH was divided into two parts:

The first part reported on the development of the anatomy based on freely available software tools and anatomical atlases (Cassola et al 2009). The second part, which is the present study, concerns dosimetric calculations for internal and external photon and electron exposure using the upright standing, mesh-based FASH and MASH phantoms. CCs for organ and tissue equivalent doses, as well as for effective doses, will be calculated and compared with corresponding data for the predecessors, the image-based, supine voxel phantoms FAX06 and MAX06 (Kramer et al 2006a), to investigate the dosimetric consequences of the anatomical differences between the two pairs of adult phantoms and also to compare the results with data available for the REX and the REGINA voxel

phantoms (Schlattl et al 2007) and for the RPI_AM and the RPI_AF mesh-based phantoms (Zhang et al 2009).

In the skeletons, dosimetry will be carried out based on μCT images of trabecular bone using methods introduced earlier (Kramer et al 2006b, 2007, 2009a, b). However, because new bone material became available, it is now possible to use μCT images of trabecular bone extracted from five representative bone sites of one adult human skeleton, which makes scaling of trabecular bone volume fractions unnecessary. In addition, improved segmentation of trabecular bone and marrow cavities will be introduced.

3. Material and methods

3.1 The FASH and MASH phantoms

Using open source software, two adult human phantoms, called FASH and MASH, have been developed based on polygon mesh surfaces (Cassola et al 2009). Instead of using images of scanned individuals, anatomical atlases and Publication 89 published by the ICRP (ICRP 2002) provided guidance for the design of organs and tissues. The development of the phantoms was necessary for two reasons: First, changing the weight of a phantom, i.e. essentially the fat distribution, is difficult to do on a voxel basis, but easy to do based on polygon mesh surfaces, for example. Second, with respect to the FAX06 and the MAX06 phantoms it was found that due to the supine position of the individuals during scanning first, the locations of the following organs were too elevated for an upright standing person: lungs, liver, stomach, small intestine (SI), colon, uterus, ovaries, urinary bladder, prostate and second, by gravitation a part of the abdominal subcutaneous adipose tissue moved laterally, thereby reducing the sagittal diameter especially in the trunk region, and adipose and muscle volumes overlying internal organs were found to be to small caused by the process of organ mass adaptation to ICRP-based data. Also, the SI was segmented in the abdomen of the FAX06 and the MAX06 phantoms with wall and contents voxels randomly distributed throughout the SI volume, because at the time it was not possible to segment the twists and turns of this walled organ. The tube

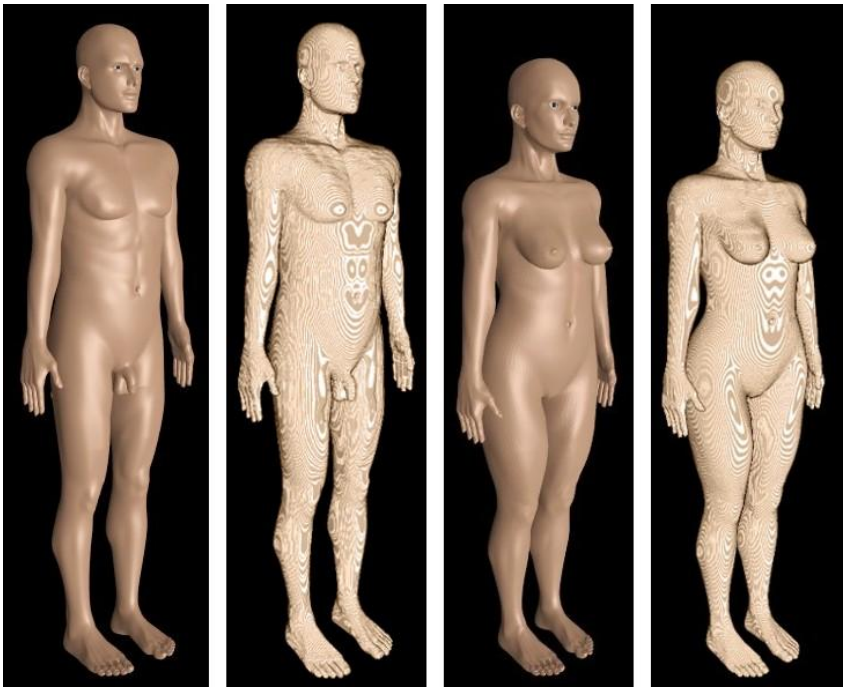

Figure 1. Surfaces: MASH polygon mesh, MASH voxelized, FASH polygon mesh and FASH voxelized, from left to right.

of the colon showed discontinuities. The connection between stomach and SI was not defined. In the skeleton, some cervical vertebrae were too thick; the pelvis was too small, especially for the female phantom and a part of the lower ribs was not clearly defined. Finally, the body shapes of the MAX06 and the FAX06 phantoms were plump and parts of their faces, like ears, eyes, noses and lips were not visible. When the list of corrections to be carried out in the FAX06 and the MAX06 phantoms continued to grow, the decision was taken to develop new phantoms to avoid these limitations right from the start instead of "meshing" the already existing voxel phantoms.

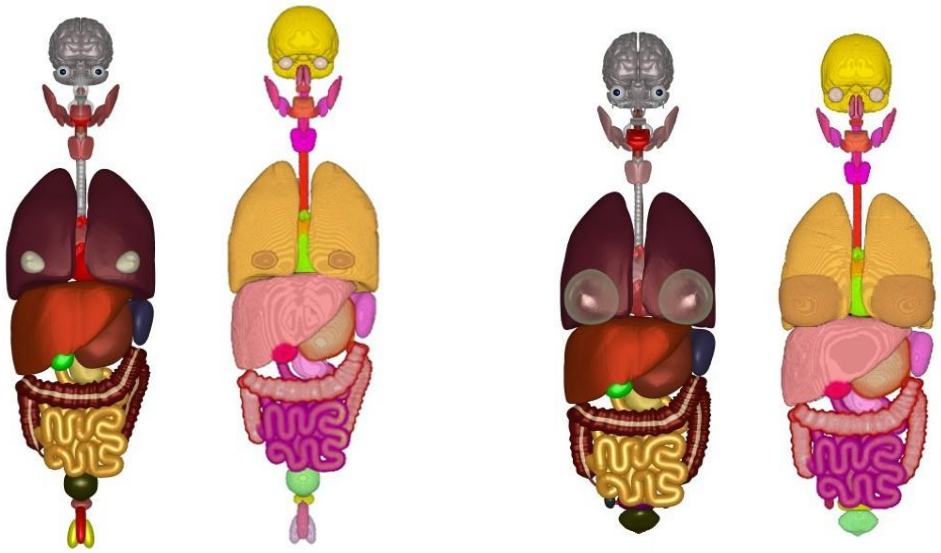

Figure 2. Organs: MASH polygon mesh, MASH voxelized, FASH polygon mesh and FASH voxelized, from left to right (Cassola et al 2009).

Figures 1 and 2 show surfaces and organs of the MASH and the FASH phantoms as polygon mesh models and as voxelized models, respectively. Voxelization is necessary, primarily because currently the EGSnrc Monte Carlo code cannot be connected directly to polygon mesh phantoms, but also because the use of μCT images of trabecular bone for skeletal dosimetry requests a voxelized phantom. The inevitable reduction of the smoothness of surfaces depends on the voxel size chosen, which is 1.2 mm x 1.2 mm x 1.2 mm for FASH and MASH, i.e. the same already used for the MAX06 and the FAX06 phantoms. Figures 1 and 2 show that this voxel size preserves the character of anatomical surfaces very well. If not stated otherwise, from here on throughout the study always the voxelized versions of the FASH and the MASH phantoms are used.

Table 1. Organs and tissues segmented in the voxelized FASH and the MASH phantoms.

Eyes	Thymus	Stomach wall	Skin
Brain	Spleen	Small intestine wall	Adipose
Spinal chord	Tongue	Colon wall	Muscle
Breasts	Nasal passage	Prostate	Skeleton*
Adrenals	Mouth cavity	Testes	Soft tissue**
Lungs	Pharynx	Penis	
Trachea	Larynx	Uterus	
Heart wall	Salivary glands	Ovaries	
Pancreas	Oesophagus	Lymphatic nodes	
Liver	Thyroid	Urinary bladder wall	
Kidneys	Gallbladder wall		

* Skeleton: Cortical bone, spongiosa, medullary yellow bone marrow, cartilage.
** Soft tissue: blood, blood vessels, connective tissue, muscular fascia, tendons, etc.

Organs and tissues of the FASH and the MASH phantoms are shown in table 1. The skeleton is composed of 19 bone sites containing segmented cortical bone, medullary yellow bone marrow, cartilage and spongiosa, which is trabecular bone filled with soft tissue. With respect to the organs and tissues relevant for the calculation of the effective dose (ICRP 2007), table 1 mentions all of them, except for the radiosensitive soft tissues located in the marrow cavities of spongiosa.

3.2 Red bone marrow and bone surface cells segmentation

The haematopoietic stem cells of the marrow, called "red bone marrow" (RBM), and the osteogenic cells on the endosteal surfaces, called "bone surface cells" (BSC) or bone endosteum are both located in the marrow cavities. The BSC represent the part of the marrow volume that is located within a distance of 10 μm from the surfaces of trabecular bone, of cortical bone neighbouring spongiosa and of medullary cortical bone, while the RBM occupies a part of the remaining marrow volume given by the cellularity factor (ICRP 1979, 1995). It was suggested that due to recent findings in radiobiology, the thickness of the bone endosteum should be increased to 50 μm (Bolch et al 2007), which apparently will be adopted by the ICRP in an upcoming report on the computational reference phantoms (ICRP 2009). Therefore, this study will consider both thicknesses for the bone endosteum.

Segmentation of RBM and BSC is a two-step process: First, the spongiosa voxels of the FASH and the MASH skeletons have to be segmented into trabecular bone and marrow. After that, RBM and yellow bone marrow (YBM) have to be segmented in the marrow cavities, while the BSC have to be defined as sub-volumes having 10 or 50 μm thickness in RBM or YBM voxels adjacent to bone surfaces.

3.2.1 Segmentation of trabecular bone and marrow cavities

To segment spongiosa voxels into trabecular bone and marrow cavities, microstructure information of human spongiosa is needed, preferably from various bone sites, to be introduced into the spongiosa voxels of the FASH and the MASH skeletons. The microstructure information used for skeletal dosimetry in the FASH and the MASH phantoms was based on μCT images of dry trabecular bone extracted from the medial section of the frontal bone, from the first lumbar vertebra (L1), from the medial section of the distal body of the sternum, between rib articular facets V and VI, from the iliac crest of the left pelvic bone and from the centre of the femoral head. The skeleton, a donation to medical science, came from an anatomical teaching collection. The subject was a female adult of 30 years, height of 1.49 m and unknown weight. The bone samples were scanned with a μCT scanner Skyscan 1172 (Skyscan Corporation, 2630 Aartselaar, Belgium) with 80 kV (100 μA) at 60 μm cubic resolution at the Imaging Laboratory of the Department of Archaeology and Anthropology, University of Bristol, Bristol, UK. Table 2 shows the dimensions of the μCT images received after scanning of the bone samples, which were the sources for trabecular microstructure information used in this study.

Table 2. Dimensions of the μCT images of the five scanned bone samples

Bone site	Number of images	Image size (pixel)
Frontal bone	271	388 x 388
Vertebra L1	534	992 x 992
Sternum	374	792 x 396
Iliac crest	305	436 x 432
Femur	674	856 x 872

In earlier studies on skeletal dosimetry based on μCT images of spongiosa (Kramer et al 2006b, 2007, 2009b), segmentation of trabecular bone and marrow in the μCT images was achieved using a histogram-based threshold function of the SCION software (SCION 2000). The problem is that one does not know how exactly SCION is segmenting the images; it is like using a black box. Therefore, a method for segmenting μCT images of spongiosa was developed based on the publication by Gonzalez and Woods (2002) and applied to the μCT images mentioned in table 2. The segmentation of trabecular bone and marrow cavities included the following steps in the spatial domain:

- Non-linear 3D median filtration with kernel size 3x3x3 to remove noise.
- Application of grey-level linear transformation functions for contrast enhancement and expansion of the 8-bit image to the interval [0,255].
- Boundary detection between the two media using a 3D Sobel filter based on first order derivative.
- Segmentation between the two tissues using a threshold value of 128.

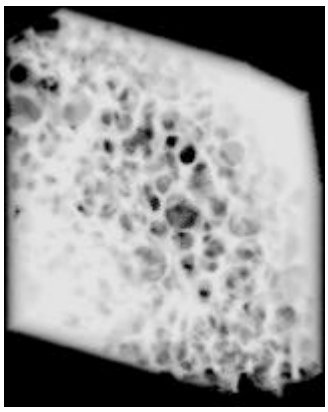

Figure 3a. Frontal bone

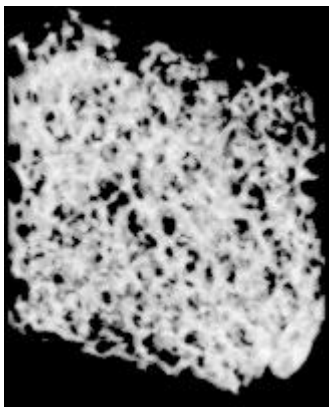

Figure 3b. Sternum

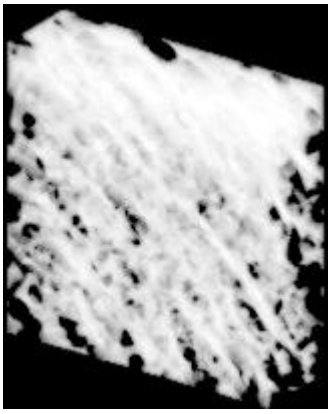

Figure 3c. Pelvis

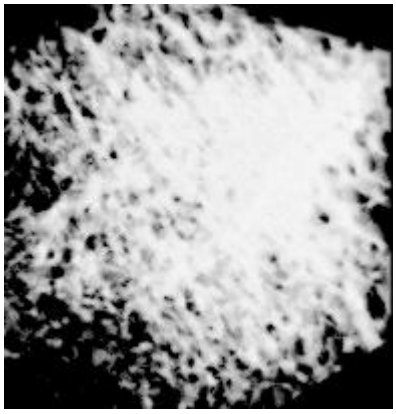

Figure 3d. Femur

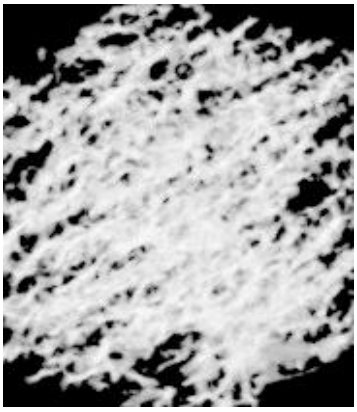

Figure 3e. Lumbar vertebra

3D representations of the segmented μCT images of the five bone samples are presented in figures 3a to 3e. One can see that the amount and the structure of bone in the spongiosa varies between different bones, and also within a specific bone, i.e. that the trabecular bone volume fraction (TBVF) is not necessarily constant everywhere in the spongiosa volume of a particular bone.

3.2.2 Introducing the microstructure information into the spongiosa voxels

Skeletal dosimetry based on segmented μCT images of spongiosa has recently been introduced to calculate RBM and BSC equivalent doses in human phantoms for external exposure to photons and internal exposure to electrons (Kramer et al 2006b, 2007, 2009a, b, Walters et al 2009). In order to use the segmented μCT images for skeletal dosimetry, spongiosa voxels in the skeletons were replaced at run time by so-called micro matrices, which have exactly the size of a spongiosa voxel and contain the requested microstructure information, i.e. segmented trabecular bone and marrow micro voxels. A cluster (= parallelepiped) of 2x2x2 = 8 micro matrices was used systematically and periodically throughout the spongiosa volume during the radiation transport calculation. Systematic means that when a particle leaves a spongiosa voxel to enter into a neighbouring spongiosa voxel, then the next micro matrix in the cluster will be used. Periodical means that if the particle travels through more than two neighbouring spongiosa voxels, the cluster will be repeated. The results have shown that a cluster with 2x2x2 = 8 micro matrices is sufficient to simulate adequately the trabecular microstructure in the spongiosa voxels of the FAX06 and the MAX06 skeletons. The technique was called the 8 SP cluster method, with '8' and 'SP' being acronyms for 'eight micro matrices' and for 'systematic-periodic', respectively. Accordingly, clusters with 8 micro matrices were extracted from the five images mentioned in table 2 and shown in figures 3a to 3e. Because of the variations of the TBVF across the spongiosa volume, care was taken to extract clusters with a TBVF close to the TBVF data found in ICRP70 (ICRP 1995). Table 3 presents the TBVFs of the clusters together with the data found in ICRP70, as well as the differences between them. Parietal and frontal bone are neighbouring bones of the skull; ribs and sternum are neighbouring bones in the ribcage.

In this study, clusters extracted from the bone sites mentioned in table 3 were used for the following bones: frontal bone for skull and mandible, vertebra L1 for spine and sacrum, sternum for sternum, ribs, clavicles and scapulae, iliac crest for pelvis and femur for arm and leg bones. It is assumed that with clusters of micro matrices extracted from these five bone sites spongiosa in the human skeleton is adequately represented for the purposes of radiation protection.

Table 3. Trabecular bone volume fractions (TBVF) for male and female adults given by ICRP70 (ICRP 1995) and for the 2x2x2 clusters used in this study.

ICRP70 Bone site	ICRP70 TBVF %	This study Bone site	This study TBVF %	Difference TBVF %
Parietal bone	55.4	Frontal bone	51.6	-3.8
Vertebrae	11.9	Vertebra L1	11.3	-0.6
Rib	10.4	Sternum	11.4	1.0
Iliac crest	19.9	Iliac crest	21.2	1.3
Femur	14.8	Femur	15.2	0.4

3.2.3 Segmentation of RBM and BSC at runtime

Having micro matrices with segmented trabecular bone and marrow cavities, the next step is to segment RBM and BSC. RBM shares the space of the marrow cavities with YBM and in addition, every 60 μm cubic marrow voxel adjacent to bone contains a 10 or 50 μm thick portion of BSC. The amount of RBM in the marrow is given by the cellularity factor (ICRP 1995), which represents the volume fraction of RBM in the marrow and which depends on age, even for adults. It seems obvious to segment RBM and YBM in the cavities of the micro matrices, particularly because with a cubic size of 60 μm the YBM micro voxels happen to match approximately the size of the 57 μm adipocytes (= fat cells) observed by Bolch et al (2002). However, segmentation between RBM and YBM would have to be repeated whenever the cellularity factor changed, which could, for example,

happen as a function of adult age or in patient-specific skeletal dosimetry. Also, as segmentation of a 10 or 50 μm BSC layer in 60 μm marrow voxels is not possible, an alternative solution for the last step of RBM and BSC segmentation had to be found.

In order to use the same μCT images segmented into trabecular bone and marrow cavities independently from actual cellularity factors, BSC layer thickness and voxel resolutions, it was decided to undertake the RBM and the BSC segmentation at runtime. In other words, the last step of segmentation does not happen in the external micro matrices, but in the internal micro matrices created by the Monte Carlo code in the computer's RAM at runtime. After reading the clusters for the five representative bone sites, the Monte Carlo code first segments RBM and YBM micro voxels in the bone marrow, taking into account that adipocytes appear mostly in groups of three fat cells (Bolch et al 2002) and cellularity factors for 40 year old adults, based on ICRP70 (ICRP 1995), which are 0.38 for skull and mandible, 0.6 for ribcage, 0.7 for spine and sacrum, 0.48 for pelvis and 0.25 for arm and leg bones. Then, an algorithm defines a 10 or 50 μm BSC layer in all segmented RBM and YBM micro voxels adjacent to trabecular bone surfaces, to cortical bone surfaces neighbouring spongiosa and to medullary cortical bone surfaces and calculates RBM and BSC volumes for all 19 bone sites. Finally, appropriate algorithms ensure that radiation energy losses are deposited in RBM micro voxels and in the BSC-part of RBM and YBM micro voxels adjacent to bone (Kramer et al 2007b, 2009a, b). The masses of the RBM and the BSC for 10 and 50 μm BSC layer thickness in the FASH and the MASH skeletons as determined by the 8 SP cluster method plus the RBM and BSC segmentation at runtime are shown in table 4 together with corresponding data found in ICRP documents for adults.

Table 4. Adult skeletal soft tissue masses according to ICRP30 (ICRP 1979) and ICRP89 (ICRP 2002) and in the phantoms FASH and MASH. The data are given for the two BSC layer thicknesses of 10 and 50 μm.

	ICRP female (g)	ICRP male (g)	FASH (g)	MASH (g)
RBM 10	900	1170	864.2	1104.7
BSC 10		120	94.1	124.4
RBM 50			768.5	981.6
BSC 50			354.3	467.4

3.3 Monte Carlo calculations

Using the EGSnrc Monte Carlo code (Kawrakow 2000a, b, Kawrakow and Rogers 2003), dosimetric calculations were carried out with the FASH, the MASH, the FAX06 and the MAX06 phantoms for external exposure to photons and for internal exposure to photons and electrons. Whole-body external exposure was simulated for anterior-posterior (AP) incidence of the radiation and for rotational (ROT) incidence, which corresponds to a full rotation of the human body around its vertical axis in a unidirectional field. According to ICRU57 (ICRU 1996), AP and ROT incidences are the most important whole-body exposure geometries in radiological protection. Gamma and beta emitters homogeneously distributed in the contents of the SI were selected as an example for internal exposure to photons and electrons. The photon cut-off energy was 2 keV in all tissues, while the electron cut-off energy was 20 keV in all tissues outside the skeleton for external exposure and 5 keV for internal exposure. In skeletal tissues the electron cut-off energy was always 5 keV. Numbers of incident or emitted particles were chosen to keep statistical errors generally below 1% for organ and tissue equivalent doses. This was not always possible for small organs and /or very low particle energies. If greater than 1%, additional information about statistical errors is given in the sections presenting the results. Organ and tissue equivalent doses for external exposure to photons were normalized to air kerma and are presented as CCs as function of the incident photon energy. For internal exposure,

results will be shown as organ and tissue absorbed energy fractions. The tissue densities and compositions were the same as those already used for the older phantoms (Kramer et al 2006a). They are based on data given in ICRU44 (1989) and ICRU46 (1992).

4. Results

4.1 External exposure to photons

Representative of the results for all organs and tissues in the FASH and the MASH phantoms, this section shows CCs for one organ and one tissue for each phantom for AP incidence, as well as for the effective dose for AP and ROT incidence. Complete sets of tabulated CCs can be found in the appendix.

4.1.1 Urinary bladder wall and RBM (FASH phantom)

Figure 4 shows CCs between equivalent doses for the urinary bladder wall and air kerma for the FAX06, the FASH and the REGINA phantoms for AP incidence and as a function of the incident photon energy. Compared to the FAX06 phantom, the FASH bladder wall equivalent dose is significantly smaller for almost the whole range of photon energies. The reason for this is the coronal shift of the bladder in the FAX06 phantom caused by the supine position of the scanned female, who provided the images for this phantom. If a person is standing, the urinary bladder is located partly behind the pubis, a bone of the pelvis, with the effect that for AP radiation incidence more than 50% of the bladder volume is shielded by bone. Figures 5a and 5b show the centre slices of the bladders in the FASH and the FAX06 phantoms, respectively. In front of the FAX06 bladder one finds only muscle, fat and soft tissue, but no bone, while the image for the FASH phantom shows a bone (pubis) right in front of the bladder. Shielding by the pubis, and also the presence of a thicker frontal layer of muscle and adipose tissue explain why the FASH bladder wall CC is smaller than the FAX06 bladder wall CC by 80%, 60%, 40%, 20% for incident photon energies of 20, 30, 40 and 70 keV. Above 70 keV up to 10 MeV this difference does not exceed 10-15%.

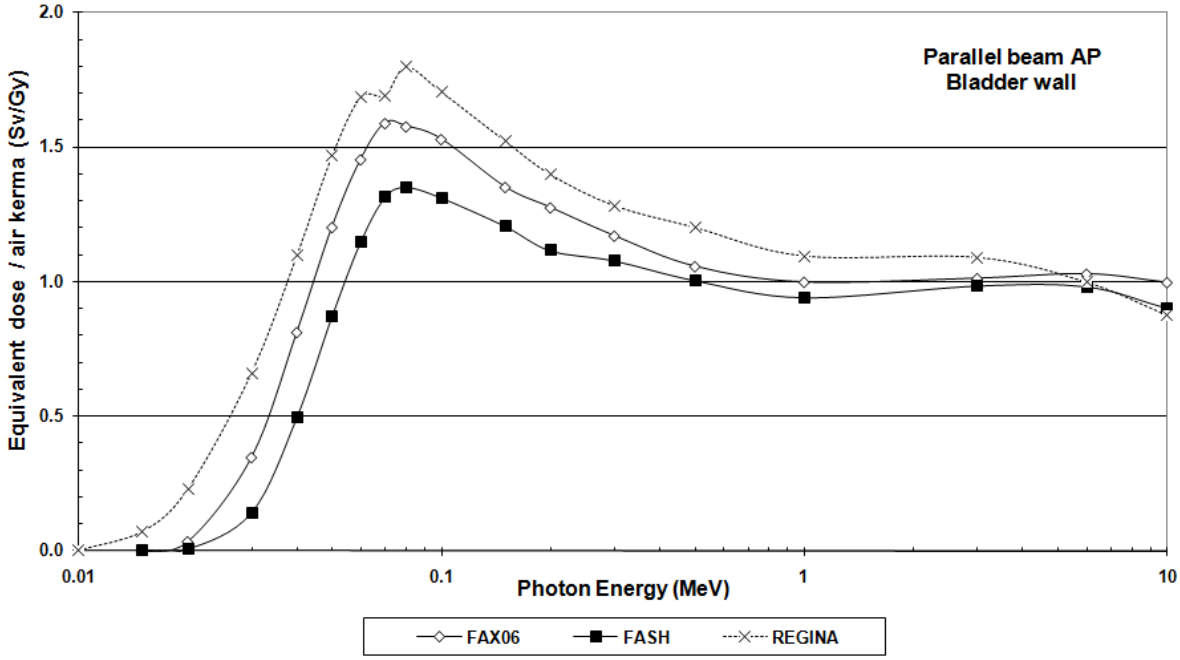

Figure 4. Bladder wall equivalent dose per air kerma for the FAX06, the FASH and the REGINA phantoms for AP incidence of monoenergetic photons as a function of the photon energy.

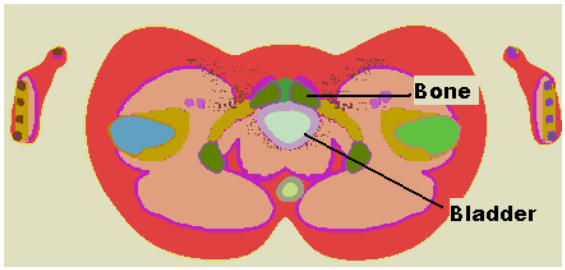

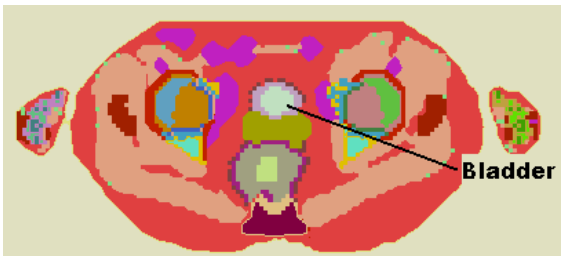

Figure 5a. Centre slice of the urinary bladder in the FASH voxelized phantom.

Figure 5b. Centre slice of the urinary bladder in the FAX06 phantom

The bladder wall equivalent dose of the REGINA phantom (Schlattl et al 2007), also shown in figure 4, is even greater than the FAX06 bladder equivalent dose. The differences between the FASH and the REGINA bladder wall CCs are 80%, 40%, 23% and 16% at 30, 50, 100 and 500 keV. This could mean that no shielding by bone occurs in front of the bladder in the REGINA phantom, and/or that the REGINA bladder is probably located also much closer to the phantom's surface. This assumption is also supported by the fact that the REGINA bladder CC for AP incidence is one of the greatest among all organ and tissue CCs, only superseded by the CC for the thyroid.

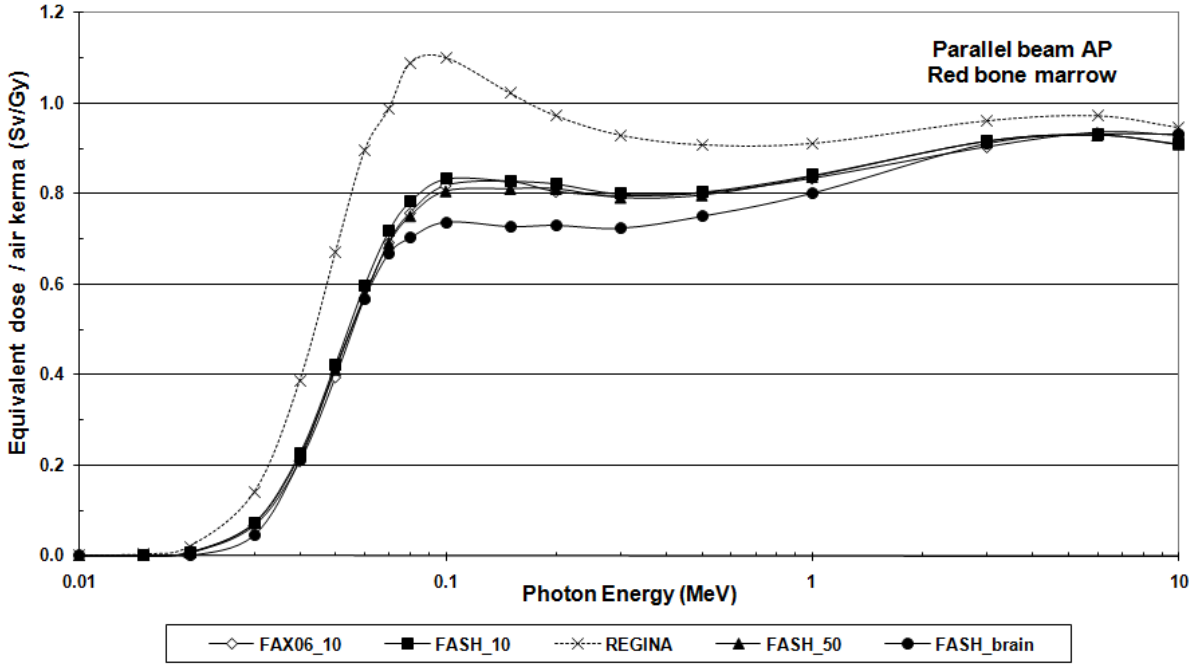

Figure 6. RBM equivalent dose per air kerma for the FAX06, the FASH and the REGINA phantoms for AP incidence of mono-energetic photons as a function of the photon energy.
The CCs for the FASH phantom are shown for the two BSC layer thicknesses of 10 and 50 μm. Additionally the brain CC for the FASH phantom is included in the figure.

Of all organs and tissues of the human body, the RBM is one among the most protected radiosensitive soft tissues. Apart from neighbouring organs and soft tissues, like adipose and muscle, the RBM is additionally shielded by a layer of cortical bone and by trabecular bone surrounding the marrow cavities. Taking these factors into account, RBM equivalent doses in the four voxel phantoms were determined using the 8 SP cluster method described above. Figure 6 shows RBM equivalent doses for external frontal whole body exposure as a function of the incident photon energy for the FAX06 and the FASH phantoms. In the calculations, 10 μm were used for the BSC layer thickness for the FAX06 and the FASH phantoms and additionally 50 μm for the FASH phantom. The results show that the FASH RBM equivalent dose is greater than the FAX06 RBM equivalent dose by 20% at

15keV, 10% at 30 keV, 5% at 60 keV and less than 1% above 150 keV because in some bones of the FAX06 skeleton the cortical bone shell was slightly thicker. A BSC layer thickness of 50 μm causes a decrease of the FASH RBM equivalent dose by up to 3.8% seen at 70 keV. Similar results for the RBM equivalent dose were also found for the MAX06 and the MASH phantoms.

Figure 6 also shows the RBM equivalent dose for the REGINA phantom, which is significantly greater than all the RBM CCs discussed above. Compared to the REGINA RBM CC, the FASH RBM CC is 80%, 37%, 24% and 12% smaller at energies of 15, 50, 100 and 500 keV, respectively. Schlattl et al (2007) applied a three correction factor (3CF) method after Zankl et al (2002) to the spongiosa voxels of the REGINA phantom. Here, spongiosa is considered to be a homogeneous mixture of marrow and bone. Energy deposited by a photon in a spongiosa voxel is multiplied by the three correction factors, which are the RBM mass fraction, the ratio between the mass-energy absorption coefficients for RBM and the spongiosa mixture and the King-Spiers factor for the dose enhancement in marrow cavities from photoelectrons released in trabecular bone. The cortical bone shell was partly not segmented in the bones of the REGINA skeleton (Zankl et al 2007), which reduces the shielding effect for the marrow in the spongiosa and consequently leads to elevated RBM equivalent doses. The King-Spiers factors were developed based on photons incident on the outer cortical bone shell of vertebrae (King and Spiers 1985), i.e. when applied to the photon energy in the spongiosa this may also lead to elevated RBM equivalent doses.

Other μCT-based RBM equivalent dose data for external photon exposure are the fluence-to-dose response (FDR) functions by Eckerman et al (2007), for example; however, those are currently not available as tables. Apart from the RBM and the BSC, the human brain is also shielded by bone, and therefore this organ is experiencing a shielding environment similar to that of the skeletal soft tissues. The brain is shielded by two layers of cortical bone with a spongiosa layer between them. Figure 6 also shows the CC for the brain of the FASH phantom, which is much closer to the RBM equivalent dose CCs for the FAX06 and the FASH phantoms than to that of the REGINA phantom, which supports the RBM equivalent doses produced by the 8 SP cluster method.

4.1.2 Lungs and BSC (MASH phantom)

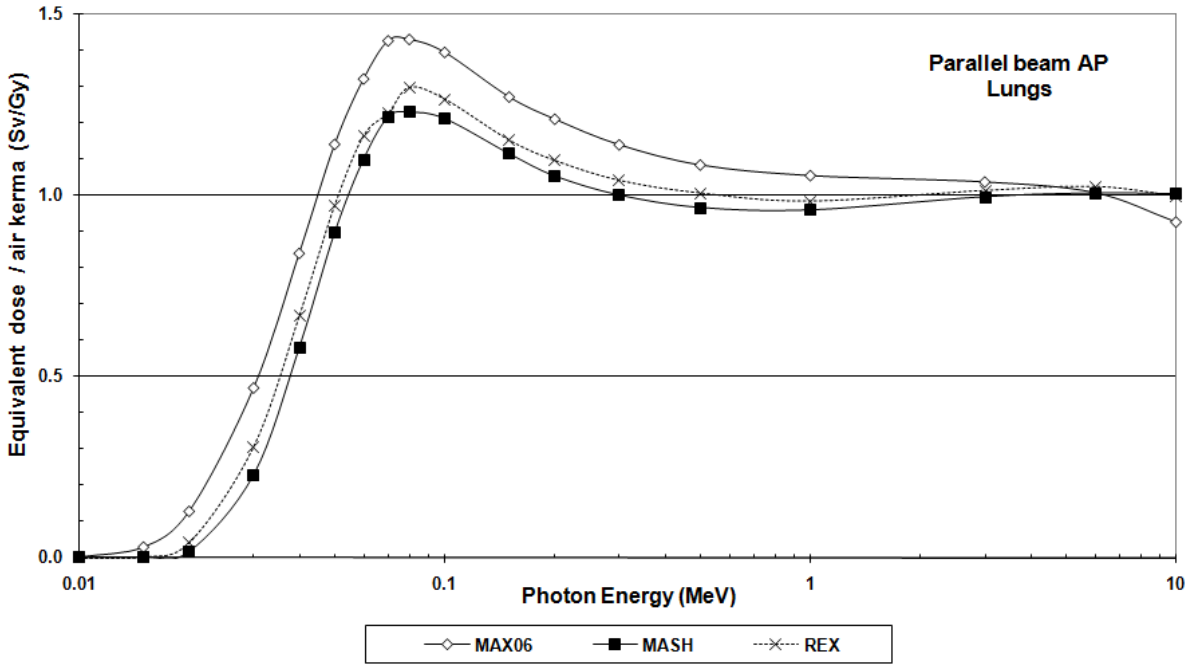

Figure 7. Lungs equivalent dose per air kerma for the MAX06, the MASH and the REX phantoms for AP incidence of mono-energetic photons as a function of the photon energy.

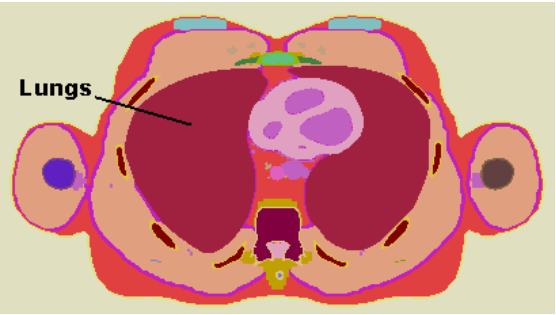

Figure 8a. Centre breast cross-section in the MASH voxelized phantom

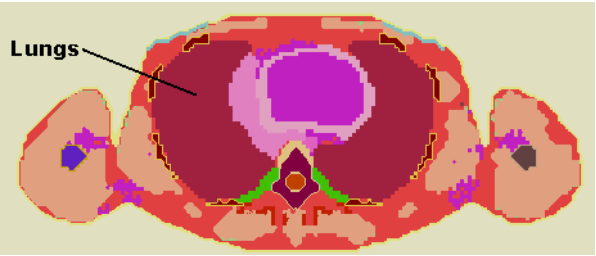

Figure 8b. Centre breast cross-section in the MAX06 phantom

Apart from different organ locations caused by the 'supine position effect', old and new phantoms differ also with respect to the thickness of the adipose and muscle layer covering some internal organs. Figure 7 shows CCs between equivalent doses for the lungs and air kerma for the MAX06, the MASH and the REX phantoms for AP incidence and as a function of the incident photon energy. The MASH CC is significantly smaller than the MAX06 CC because of a thicker layer of muscle and adipose tissue shown in figures 8a and 8b, which demonstrates that modelling of the human anatomy can have significant dosimetric consequences. If a voxel phantom should have organ and tissue masses in agreement with ICRP89, organ volumes are enlarged or made smaller usually by exchanging organ voxels with adjacent tissues, like adipose, muscle or unspecified soft tissue. If at the same time the boundaries of the body, as given in the digital images, remain unchanged, it is possible that the volume adjustment of organs may be achieved at the expense of the adjacent tissues, i.e. their volumes could become too small in certain regions of the body. With mesh-based phantoms this problem does not exist, because only after all the internal organs have been developed and fitted into the skeleton, are muscle and adipose tissues added and the surface adjusted if necessary. The reduction of lung equivalent dose in the MASH phantom is 88%, 22% and 15% at 20, 50 and 100 keV. Between 100 keV and 10 MeV this difference ranges between 10 and 15%. With respect to the REX lung CC, these differences are 63%, 8% and 4% at the same energies.

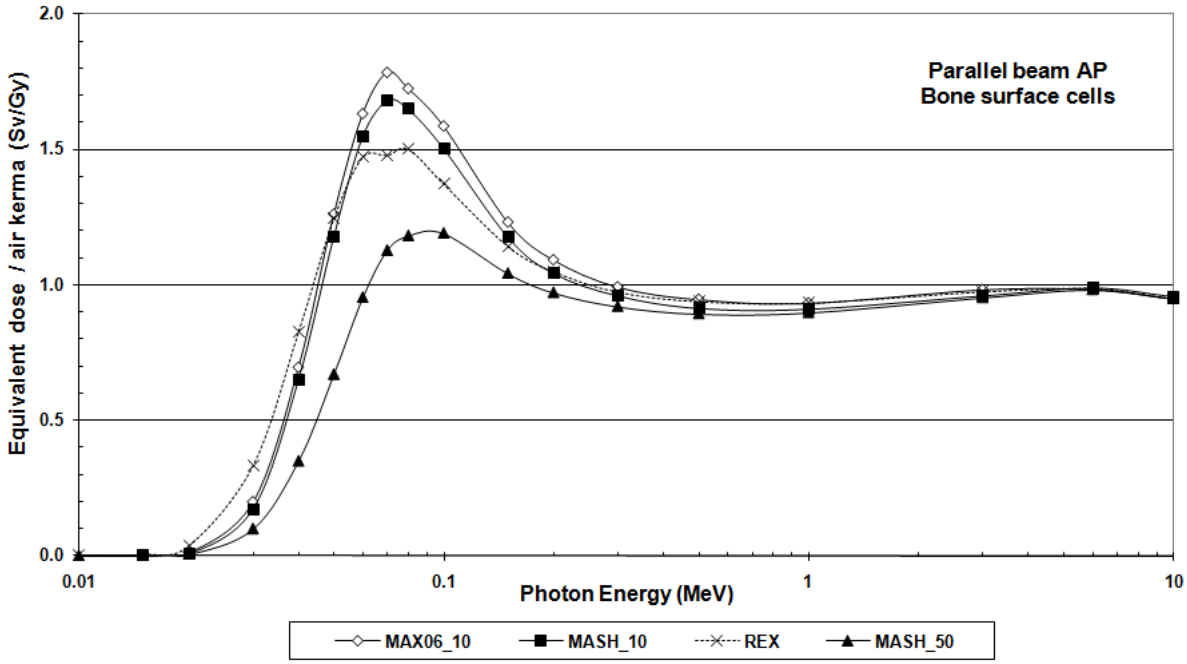

Figure 9. BSC equivalent dose per air kerma for the MAX06, the MASH and the REX phantoms for AP incidence of mono-energetic photons as a function of the photon energy. The CCs for the MASH phantom are shown for the two BSC layer thicknesses of 10 and 50 μm.

Figure 9 shows CCs between equivalent doses for the BSC and air kerma for the MAX06, the MASH and the REX phantoms for AP incidence and as a function of the incident photon energy. Again, a BSC layer thickness of 10 μm was used for the MAX06 and the MASH phantoms and additionally 50 μm for the MASH phantom. The MASH CC is smaller than the MAX06 CC because in the MASH phantom organs and tissues, and also the skeleton, are more shielded by overlying muscle and adipose. The differences are smaller than 5% for incident photon energies above 60 keV, while for lower energies the difference between the BSC CCs for the two phantoms can rise to 75% at 15 keV.

Being located next to the RBM in the marrow cavities, the BSC consequently experience the same shielding environment. Nevertheless, over the whole range of incident photon energies, BSC equivalent dose CCs shown in figure 9 are significantly greater than corresponding RBM equivalent dose CCs, like those shown in figure 6. For 10 μm BSC layer thickness, the BSC CC is more than 100% greater than the RBM CC in the region of the maximum, around 70 keV, for example. In order to understand this remarkable phenomenon one has to track the secondary electrons with respect to the tissues, where these electrons have been released by photon interactions.

Figure 10 shows on a logarithmic scale the "Total" BSC CC, already seen in figure 9 as MASH_10, and separately the contributions to the BSC equivalent dose from electrons originating in the marrow, the trabecular and the cortical bone and in tissues located outside the skeleton. Marrow electrons are the major contributor to the BSC equivalent dose up to 20 keV. Then, secondary electrons released in trabecular bone dominate energy depositions in the 10 μm BSC layer up to 100 keV, where the contributions from trabecular and marrow electrons become equal again. For higher photon energies, the marrow electrons remain the dominant contributor to the BSC equivalent dose. For the MASH phantom, the marrow component of the BSC equivalent dose agrees with the RBM equivalent dose within 15%, i.e. that the significantly greater equivalent dose in the BSC layer is caused by photoelectrons released in trabecular bone entering the marrow cavities.

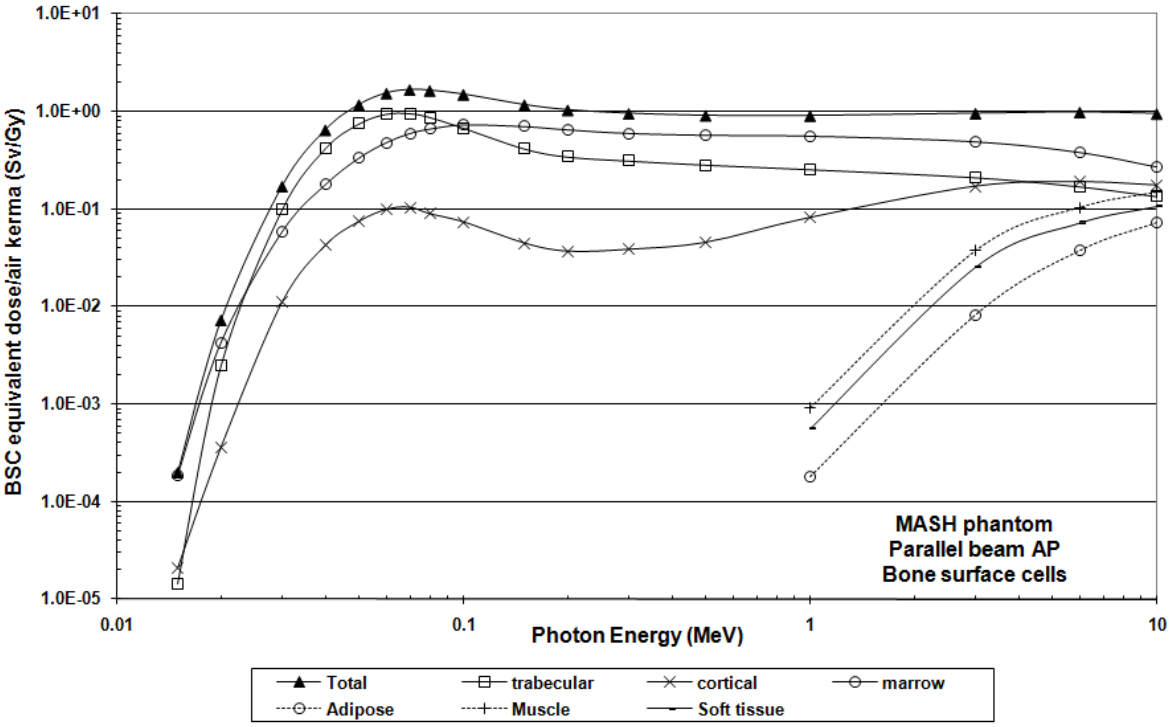

Figure 10. Total BSC equivalent dose per air kerma for the MASH phantom for AP incidence of mono-energetic photons as a function of the photon energy and for 10 μm BSC layer thickness. Additionally the contributions from electrons released in marrow, in trabecular bone, in cortical bone and in soft tissues located outside the skeleton are shown.

The greatest difference between the trabecular and the marrow contribution was found at 40 keV, where the BSC equivalent dose caused by trabecular photoelectrons supersedes the BSC equivalent dose caused by marrow electrons by a factor of 2.3. At the maximum of the total curve at 70 keV, the trabecular component is still 60% greater than the marrow component.

Because of the limited range of electrons with energies below 100 keV in soft tissue, the flux of trabecular photoelectrons into the marrow cavities has a significant effect only in the 10 µm layer adjacent to the bone surface, and not in the remaining volume of the marrow cavities with diameters of hundreds of µm. Figure 9 shows that the increase of the BSC layer thickness to 50 µm leads to a decrease of the BSC equivalent dose; however, the equivalent dose enhancement effect remains visible. This decrease occurs because energy depositions by electrons per unit length rapidly decrease as a function of the distance travelled in the marrow. The BSC equivalent dose enhancement is a low energy phenomenon because it is based on photoelectrons released in bone, which enter the marrow cavities. As the production of secondary Compton electrons does not depend on the material density like the photo-electric effect, the enhancement of the BSC equivalent dose disappears with increasing photon energy when the photo-electric effect becomes negligible.

Figure 9 also shows the BSC equivalent dose for the REX phantom, which actually represents the average equivalent dose to the spongiosa, because Schlattl et al (2007) did not use a specific method to calculate the equivalent dose to a 10 or 50 µm layer of the BSC.

4.1.3 Effective dose

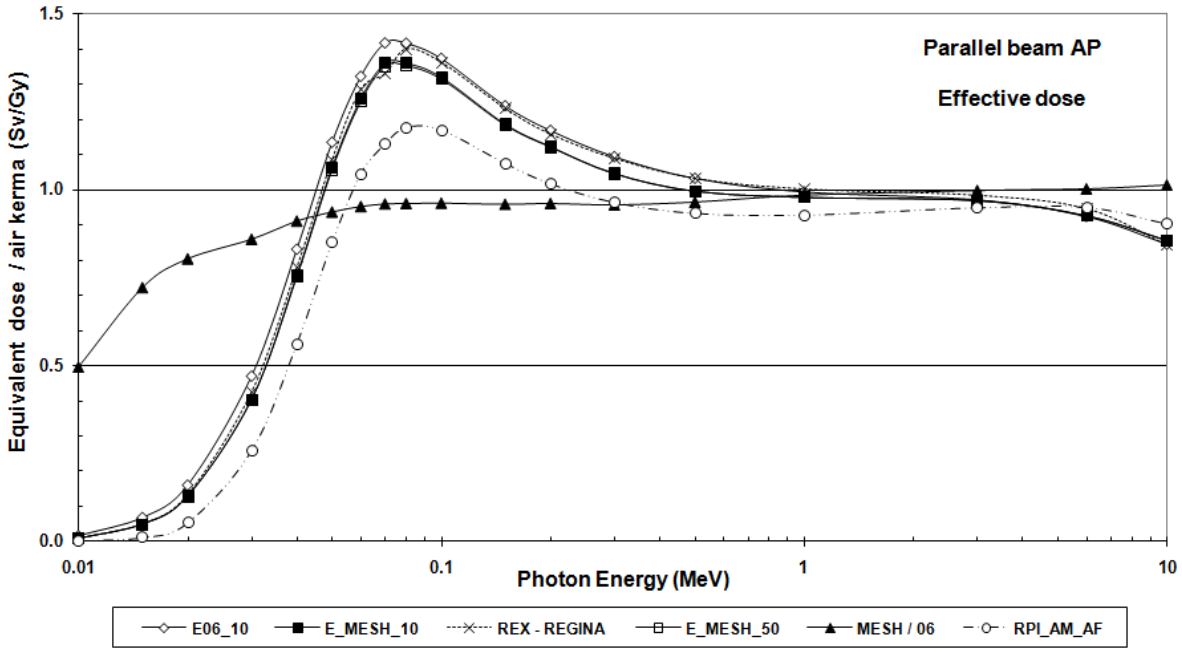

Figure 11. Effective dose per air kerma for the FAX06/MAX06, the FASH/MASH, the REGINA-REX and the RPI_AM_AF phantoms for AP incidence of mono-energetic photons as a function of the photon energy.

Figure 11 presents effective doses per air kerma E06_10 and E_MESH_10, calculated with the adult phantoms FAX06/MAX06 and FASH/MASH, respectively, with 10 µm BSC layer thickness for AP incidence of a broad parallel beam of photons as function of the incident photon energy.

E_MESH_50 is the effective dose for the FASH/MASH phantoms calculated with 50 μm BSC layer thickness, REGINA-REX represents the effective dose for the ICRP reference phantoms (Schlattl et al 2007) and RPI_AM_AF the effective dose for the RPI_AM and RPI_AF phantoms (Zhang et al 2009).

The ratio MESH / 06 shows that the effective dose CC for the FASH/MASH phantoms is smaller than the effective dose CC of the FAX06/MAX06 phantoms for almost all incident energies because organs and tissues in the mesh-based phantoms are more shielded by muscle and adipose. The differences are less than 5% for photon energies above 60 keV, while for lower energies this difference can rise to 50% at 10 keV. Using 50 μm for the BSC layer thickness has almost no effect on the effective dose compared to its value for 10 μm BSC layer thickness. The differences are smaller than 1 % for all energies. The REGINA/REX effective dose agrees well with the FASH /MASH effective dose up to 70 keV. For higher energies better agreement can be seen with the FAX06/MAX06 effective dose. Differences between E_MESH_10 and REGINA-REX never exceed 5% for all energies, except for 10 keV for which the difference is 23%. For most of the incident photon energies, the RPI_AM_AF effective dose is significantly smaller than all other effective doses. Differences are 60 – 15% between 30 and 100 keV and factors of 2.5 – 4.2 for lower energies. Above 100 keV differences between RPI_AM_AF and the other effective doses are 10-15%.

Figure 12 presents corresponding effective doses E06_10, E_MESH_10, E_MESH_50, REGINA-REX and RPI_AM_AF for ROT incidence of a broad parallel beam of photons as function of the incident photon energy. As for the phantoms FASH, MASH, FAX06 and MAX06, again, the differences between E06 and E_MESH_10 are less than 5% for energies above 60 keV, while for lower energies this difference can raise to 40% at 10 keV. Up to 80 keV the REGINA-REX effective dose shows values just between the data for E06 and E_MESH. Between 80 and 500 keV agreement with E06 is better, while for higher energies the REGINA-REX effective dose is greater than E06 as well as E_MESH. Differences between E_MESH_10 and REGINA-REX never exceed 5% for all energies, except for 10 keV for which the difference is 24%. Again, the RPI_AM_AF effective dose

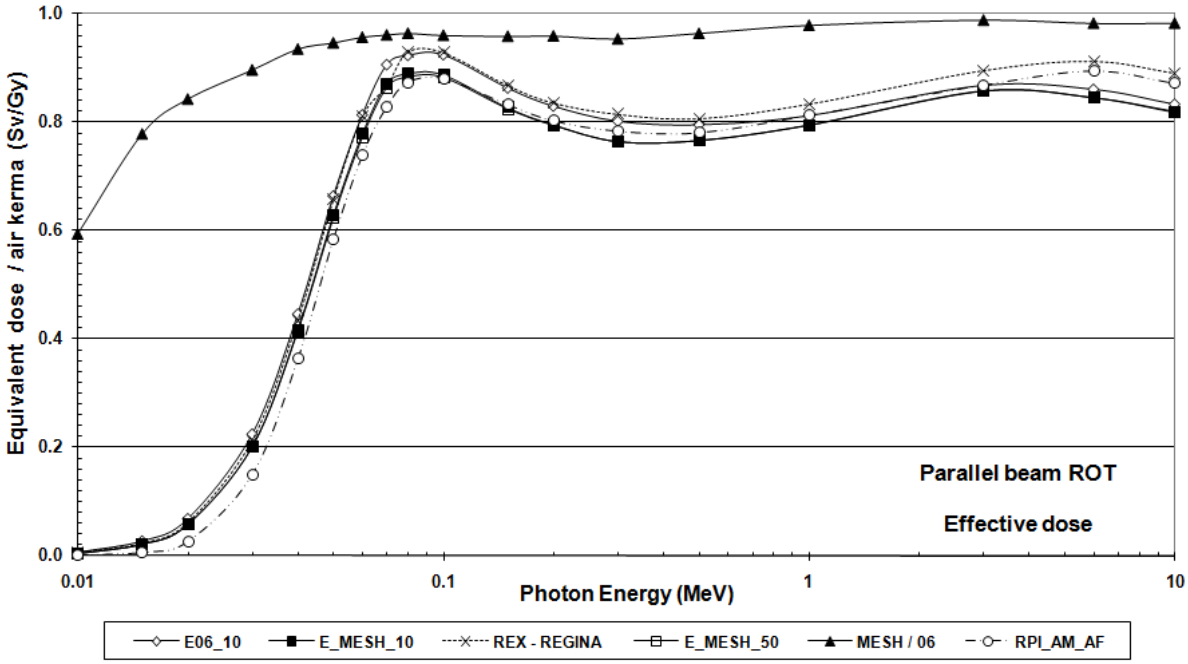

Figure 12. Effective dose per air kerma for the FAX06/MAX06, the FASH/MASH, the REGINA-REX and the RPI_AM_AF phantoms for ROT incidence of mono-energetic photons as a function of the photon energy.

is smaller than all other effective doses, but now only for energies up to 80 keV and the differences are smaller: 40 – 5% for energies between 30 and 100 keV and factors of 2.2 to 3.2 for lower energies. Zhang et al (2009) also report CCs for the testes, the male RBM, the female breasts and the ovaries. A comparison with FASH/MASH results given in the annex of this study for AP incidence shows agreement within 5-10% for the testes and the male RBM for energies above 50 keV, but differences of factors up to 8.6 at 15 keV for the female breasts and up to 1.75 at 30 keV for the ovaries, both being organs which contribute with high tissue weighting factors to the effective dose. In contrast to the RPI_AF phantom, but similar to the REGINA phantom, in the FASH phantom's breasts fat and glandular tissue are not separated, which causes greater breast equivalent doses for AP incidence in the FASH phantom as compared to the RPI_AF phantom, whose breasts contain a shielding of fat located around the glandular tissue. Female breast equivalent doses for FASH and REGINA agree within a margin of 5% for photon energies above 15 keV and AP incidence. FASH and RPI_AF ovaries are located at similar distances from the frontal surface. Therefore, differences between corresponding ovary equivalent doses cannot be explained for the time being. As for the explanation of the effective dose differences one would have to compare additionally all other organ and tissue CCs for all phantoms, because differences between breast equivalent doses alone cannot explain the effective dose differences found.

4.2 Internal exposure

In the FAX06 and the MAX06 phantoms, the SI was represented in the abdomen by a volume with randomly distributed wall and contents voxels, because it was too complicated to segment wall and contents with all its characteristic twists and turns on a voxel basis. In the FASH and MASH phantoms this problem was resolved by using polygon mesh surfaces and it is now interesting to find out what the dosimetric implications of this anatomical improvement could be.

Figures 13a and 13b show frontal views of the colon and the SI, while figures 14a and 14b present cross-sections through the lower abdomen for the FASH and the FAX06 phantoms, respectively. The improvements of the anatomical representation of the SI, and also of the colon, in the FASH phantom are obvious. The FASH SI has a wall thickness of 0.6 cm and the diameter of the contents is 1.0 cm. In the SI wall, absorbed energy fractions (AFs) were calculated for mono-energetic gamma and beta emitting radionuclides with energies between 10 keV and 4 MeV, homogeneously distributed in the contents of the SI. The source particles were emitted isotropically. The cut-off energies were 2 keV for photons and 5 keV for electrons.

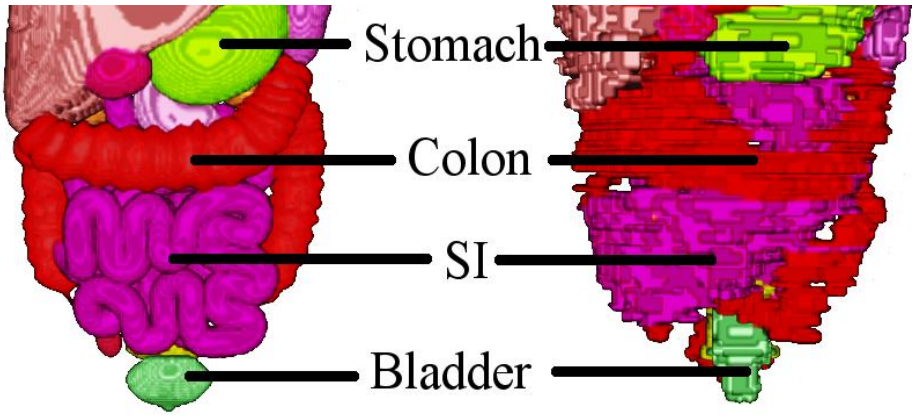

Figure 13a. FASH voxelized: Frontal view of abdominal organs

Figure 13b. FAX06: Frontal view of abdominal organs

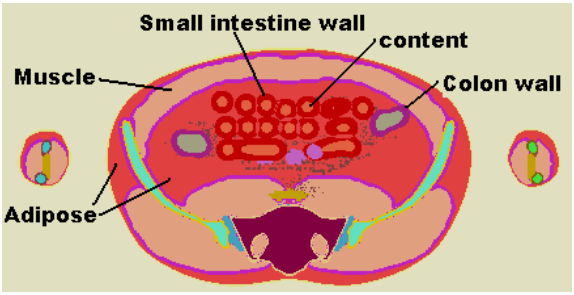

Figure 14a. FASH voxelized: Cross-section of lower abdomen

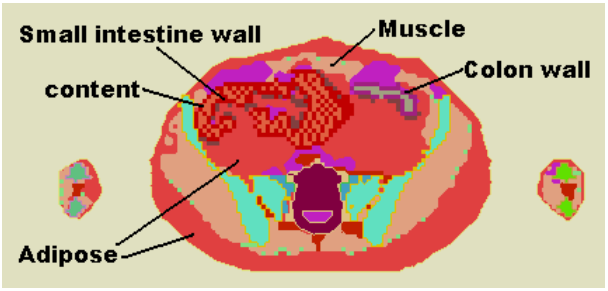

Figure 14b. FAX06: Cross-section of lower abdomen

Figure 15 shows AFs for the SI wall of the FAX06 and the FASH phantoms, when a photon emitter is homogeneously distributed in the SI content. At 10 keV, the FASH AF is only 0.19, because with a mean free path-length of 0.13 cm in soft tissue, 10 keV photons emitted in the 1 cm-thick volume of the contents are easily absorbed still in that volume. The maximum of the AF is 0.4 and occurs at almost 20 kev emitted photon energy. For 20 keV, the mean free path-length of photons is 0.84 cm in soft tissue, which gives them a greater chance to interact and consequently make energy depositions in the 0.6 cm-thick SI wall. For energies above 20 keV, photons emitted in the contents increasingly make interactions beyond the walls of the SI, which causes the AF to decrease. Only 10% of the emitted energy is absorbed in the SI wall at 70 keV and at 4 MeV this fraction has reached 4.2%. With a value of 0.3 at 10 keV, the FAX06 AF is almost 60% greater, because the random distribution of wall and contents voxels implies that a photon starting from a contents voxel will reach a neighbouring wall voxel after travelling 0.12 cm, which is the size of the cubic voxels of the phantom. The maximum of the FAX06 AF occurs also at almost 20 keV, but afterwards, with increasing energy, the decrease is stronger than for the FASH AF. For energies above 30 keV, the FASH AF in the SI wall is on average 15% greater than the FAX06 AF.

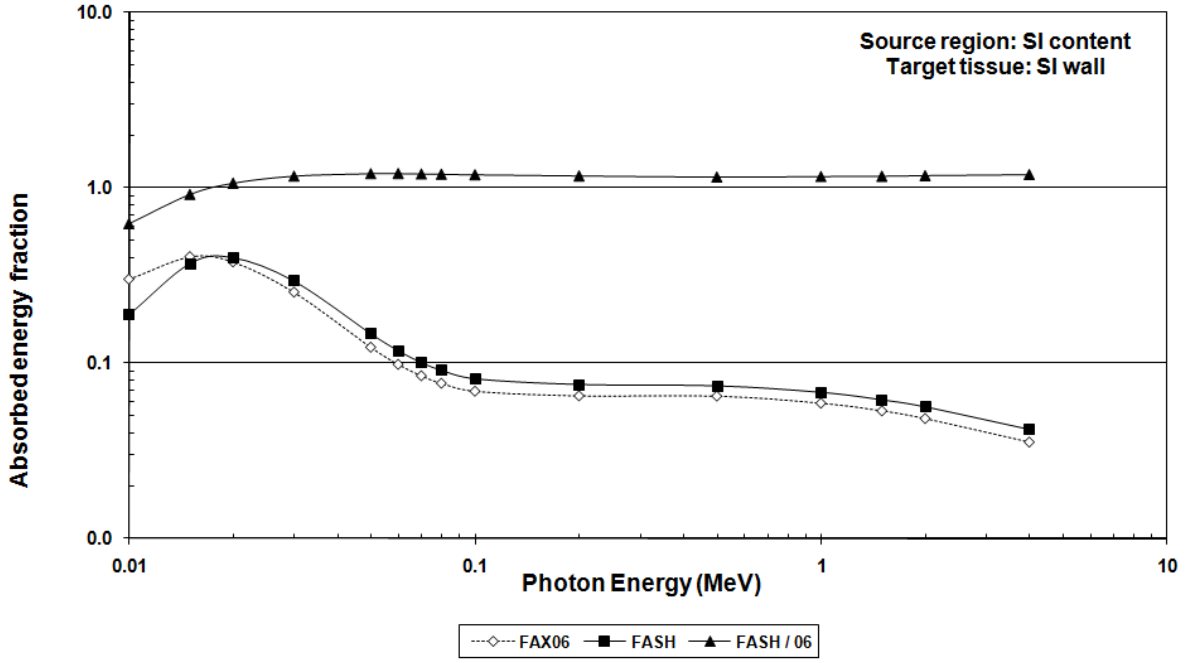

Figure 15. Absorbed energy fractions (AFs) in the SI of the FASH and the FAX06 phantoms for photons emitted isotropically in the contents of the SI as function of the emitted photon energy. FASH / 06 represents the ratio between the two AFs.

Figure 16 shows the same exposure scenario for an electron emitter; however, here the FASH AF is smaller than the FAX06 AF by 50% for emitted energies up to 1 MeV and only at 4 MeV do the two AFs become almost equal. The ranges of electrons in soft tissue are 2.5 μm at 10 keV, 0.18 cm at 500 keV and 0.98 cm at 2 MeV. This explains first of all, why for both phantoms the initial electron AFs at 10 keV have values by three orders of magnitude smaller than the initial photon AFs shown in figure 15. In addition these ranges also explain the high value of 50% difference between the two AFs, because while many electrons starting in the coherent contents of the FASH SI are absorbed still in the content, electrons starting in randomly distributed contents voxels of the FAX06 SI have to travel only a small distance to enter a neighbouring wall voxel. In other words, the argument made above for the FAX06 photon AF at 10 keV applies here again, but now for all energies up to 1 MeV. Thus, for electrons emitted in the contents of the SI, the model used in the FAX06 phantom overestimated the SI wall AF by 100%.

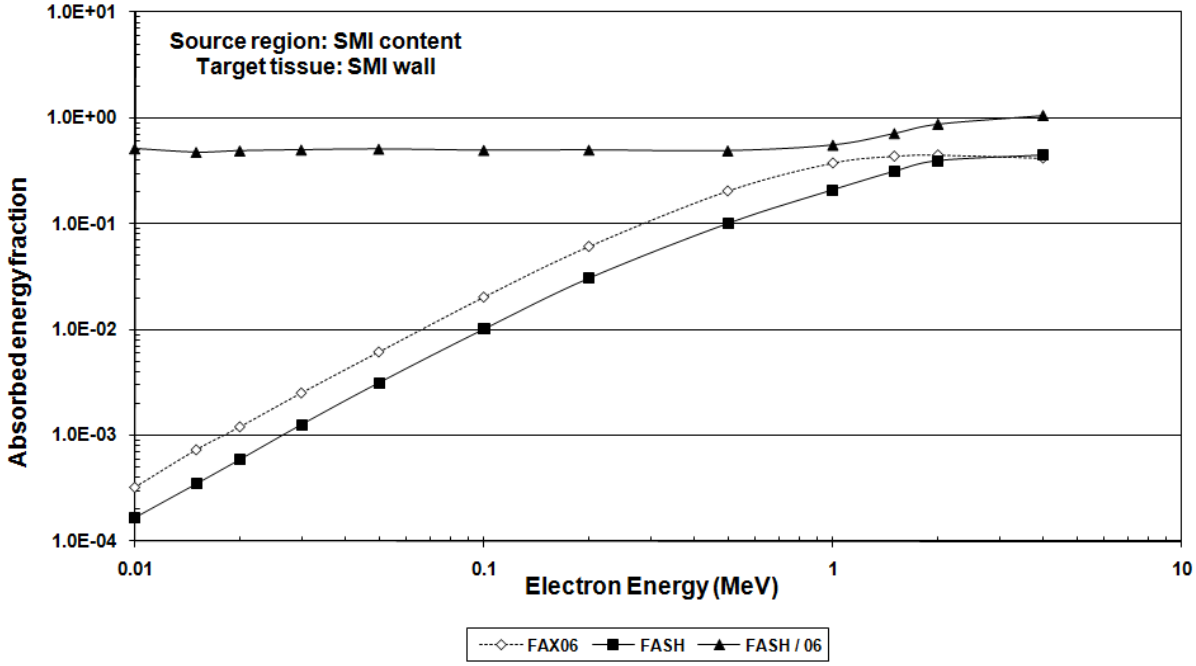

Figure 16. Absorbed energy fractions (AFs) in the SI of the FASH and the FAX06 phantoms for electrons emitted isotropically in the contents of the SI as function of the emitted electron energy. FASH / 06 represents the ratio between the two AFs.

5. Conclusion

In the first part of this study, adult human phantoms have been introduced based on polygon mesh surfaces using software tools developed in the area of computer graphics and animated film. Instead of using digital images of patients, volunteers or cadavers usually scanned in a supine position, this method applies anatomical atlases to the process of building the human body and its organs in standing posture.

The second part of this paper, the study presented here, investigated the dosimetric consequences of the anatomical differences between the adult mesh-based phantoms FASH and MASH and their predecessors, the image-based adult voxel phantoms FAX06 and MAX06. For this purpose, Monte Carlo simulations were carried out with the four phantoms for external and internal exposure to photons and electrons. Taking advantage of the introduction of the mesh-based phantoms, FASH and MASH were “equipped” with one of the most advanced techniques for skeletal dosimetry.

The comparison between the mesh-based and the image-based anatomies was made in terms of organ equivalent dose, simulating occupational exposure scenarios for external photon irradiation and internal exposure to photons and electrons in the contents of the SI. Some results were also compared with corresponding data for REGINA and REX, the ICRP adult reference phantoms and with the RPI_AM and RPI_AF phantoms. The results have shown that when the image-based, supine FAX06 and MAX06 phantoms were replaced by the upright standing FASH and MASH phantoms, organ equivalent doses differed for external exposure to photons by up to 8o% for broad beam AP irradiation. Differences of up to 50% for the effective dose for AP irradiation were observed and the equivalent dose to the SI wall from electron emitters in the contents may vary by 100%. Similar percentage differences were observed for external exposure when results for the FASH and the MASH phantoms were compared with corresponding data for the REGINA and the REX phantoms. Effective doses calculated with FASH/MASH and REGINA-REX agree for most energies and geometries within 10%, whereas the RPI_AM_AF effective doses are smaller than the other two, reaching differences of a factor of 4 for low photon energies and AP incidence. These differences could partly be explained with anatomical differences between the phantoms considered.

The phantoms FASH and MASH were not developed to just correct anatomical shortcomings of the FAX06 and the MAX06 phantoms. FASH and MASH are adult male and female phantoms with average weight and average height, designed to be used as base phantoms for the development of 16 adult phantoms for each sex, covering 4 different weights and 4 different heights in both groups. The modifications of weight and height are difficult to make based on voxels, but easy to make based on polygon mesh surfaces, which explains why the FASH and the MASH phantoms have been developed in the first place. The 32 phantoms will, for example, be used to calculate conversion coefficients for radiographic examinations, in order to be applied to the CALDose_X software (Kramer et al 2008). This would allow for patient-specific absorbed dose calculations for X-ray diagnosis.

6. Acknowledgement

The authors would like to thank the Conselho Nacional de Desenvolvimento Científico e Tecnológico - CNPq and the Fundação de Amparo à Ciência do Estado de Pernambuco - FACEPE for financial support.

7. References

Blender 2009 http://www.blender.org/ Last access June 2009

Bolch W E, Patton P W, Rajon D A, Shah A P, Jokisch D W and Inglis B A 2002 Considerations of Marrow Cellularity in the 3-Dimensional Dosimetric Models of the Trabecular Skeleton *J Nucl Med* **43**, *No.1, 97- 108*

Bolch W E, Shah A P, Watchman C J, Jokisch D W, Patton P W, Rajon D A, Zankl M, Petoussi-Henss N and Eckerman K F 2007 Skeletal Absorbed Fractions for Electrons in the Adult Male: Considerations of a Revised 50-mm Definition of the Bone Endosteum *Rad.Prot.Dos*. **127** 169-173

Cassola V F, de Melo Lima V J, Kramer R and Khoury H J 2009 FASH and MASH: *F*emale and *M*ale Adult human phantoms based on polygon me*SH* surfaces. Part I: Development of the anatomy *Phys Med Biol* **55** 133-162

Cristy M 1980 Mathematical phantoms representing children at various ages for use in estimates of internal dose *Report ORNL/NUREG/TM-367, Oak Ridge National Laboratory, Oak Ridge, Tenn., USA*

Eckerman K F, Bolch W E, Zankl M and Petoussi-Henss N, 2007 Response functions for computing absorbed dose to skeletal tissues from photon irradiation *Rad Prot Dos **127** 187-191*

Gonzalez R C and Woods R E 2002 Digital Image Processing, 2nd edition, Prentice Hall, USA

ICRP 1979 Limits for Intakes of Radionuclides by Workers *ICRP Publication 30* (Oxford: Pergamon)

ICRP 1995 Basic Anatomical and Physiological Data for use in Radiological Protection: The Skeleton. *ICRP Publication 70* (Oxford: Pergamon)

ICRP 1996 Conversion Coefficients for use in Radiological Protection against External Radiation. ICRP Publication 74 *International Commission on Radiological Protection, Pergamon Press, Oxford*

ICRP 2002 Basic Anatomical and Physiological Data for Use in Radiological Protection: Reference Values *ICRP Publication 89* (Oxford: Pergamon)

ICRP 2007 Recommendations of the International Commission on Radiological Protection *ICRP Publication 103 Ann. ICRP 37 (2-3) Elsevier Science Ltd., Oxford*

ICRP 2009 The ICRP Reference Computational Phantoms for the Adult Male and Female *ICRP Publication 108 (in press)*

ICRU 1989 Tissue Substitutes in Radiation Dosimetry and Measurement *ICRU Report No. 44* International Commission On Radiation Units And Measurements, Bethesda, MD, USA

ICRU 1992 Photon, Electron, Proton and Neutron Interaction Data for Body Tissues *ICRU Report No. 46* International Commission On Radiation Units And Measurements, Bethesda, MD, USA

ICRU 1998 Conversion Coefficients for use in Radiological Protection against External Radiation. *ICRU Report No. 57* International Commission On Radiation Units And Measurements, Bethesda, MD, USA

ImageJ 2009 National Institute of Health. ImageJ: Image Processing and Analysis in Java http://rsbweb.nih.gov/ij/index.html Last access June 2009

Kawrakow I 2000a Accurate condensed history Monte Carlo simulation of electron transport. I. EGSnrc, the new EGS4 version, *Med.Phys.* **27**, 485-498

Kawrakow I 2000b Accurate condensed history Monte Carlo simulation of electron transport. II. Application to ion chamber response simulations, *Med.Phys.* **27**, 499-513

Kawrakow I and Rogers D.W.O. 2003 The EGSnrc code system: Monte Carlo simulation of electron and photon transport, *NRC Report PIRS-701*

King S D, Spiers F W 1985 Photoelectron enhancement of the absorbed dose from X rays to human bone marrow: experimental and theoretical studies, *Br. J. of Radiol. **58**, 345-356*

Kramer R, Zankl M, Williams G, Drexler G 1982 The Calculation of Dose from External Photon Exposures Using Reference Human Phantoms and Monte Carlo Methods. Part I: The Male (ADAM) and Female (EVA) Adult Mathematical Phantoms *GSF-Report S-885.Reprint July 1999.Institut fuer Strahlenschutz, GSF-Forschungszentrum fuer Umwelt und Gesundheit, Neuherberg-Muenchen*

Kramer R, Khoury H J, Vieira J W and Lima V J M 2006a MAX06 and FAX06: Update of two adult human phantoms for radiation protection dosimetry *Phys. Med. Biol.* **51** 3331-3346

Kramer R, Khoury H J, Vieira J W and Kawrakow I 2006b Skeletal dosimetry in the MAX06 and the FAX06 phantoms for external exposure to photons based on vertebral 3D-microCT images *Phys.Med.Biol.* **51** 6265-6289

Kramer R, Khoury H J, Vieira J W and Kawrakow I 2007 Skeletal dosimetry for external exposure to photons based on CT images of spongiosa from different bone sites *Phys.Med.Biol.* ***52*** *6697-6716*

Kramer R, Khoury H J and Vieira J W 2008 CALDose_X a software tool for the assessment of organ and tissue doses, effective dose and cancer risk in diagnostic radiology *Phys. Med. Biol.* **53** 6437-6459

Kramer R, Khoury H J, Vieira J W, Robson-Brown K and Fuelle D 2009a Electron absorbed fractions in skeletal soft tissues based on red bone marrow segmentation at runtime in microCT images of human trabecular bone *World Congress 2009 – Medical Physics and Biomedical Engineering, 7-12 September 2009, Munich, Germany.*

Kramer R, Khoury H J, Vieira J W and Robson Brown K A 2009b Skeletal dosimetry for external exposures to photons based on μCT images of spongiosa: Consideration of voxel resolution, cluster size and medullary bone surfaces *Med Phys* **36** (11) 5007-5016

Lee C, Lodwick D, Hasenauer D, Williams J L, Lee C and Bolch W E 2007 Hybrid computational phantoms of the male and female newborn patient: NURBS-based whole-body models *Phys. Med. Biol .****52*** *3309-3333*

MakeHuman 2009 http://www.makehuman.org/blog/index.php Last access June 2009

Min P 2009 Binvox: 3D mesh voxelizer, http://www.google.com/search?q=binvox Last access June 2009

Na Y H, Zhang J and Xu X G 2008 A Mesh-Based Anatomical Deformation Method for Creating Size-adjustable Whole-body Patient Models. Med. Phys., Vol 35(6), 2665

SCION Image for WINDOWS 2000 Scion Corporation, www.scioncorp.com

Schlattl H, Zankl M and Petoussi-Henss N 2007 Organ dose conversion coefficients for voxel models of the reference male and female from idealized photon exposures *Phys Med Biol* ***52*** *2123-2145*

Santos C E and Frère A F 2007a Criação de um fantoma computacional multi-uso baseado em modelagem 3D, XII Congresso Brasileiro de Física Médica, Foz do Iguaçu, June 6-9 (available at http://www.abfm.org.br/c2007/pdf/B_152.pdf)

Santos CE and Frère A F 2007b Desenvolvimento de um novo tipo de fantoma baseado em modelagem 3D, VII Workshop de Informática Médica (WIM 2007), Porto de Galinhas June 25-26 (available at http://www.ime.uerj.br/professores/cecas/AnaisWIM2007/sessao5/4-28371.pdf)

Snyder W S 1950 Calculations for maximum permissible exposure to thermal neutrons *Nucleonics* ***6****, 2, 46-50*

Snyder W S, Ford M R and Warner G G 1978 Estimates of absorbed fractions for monoenergetic photon sources uniformly distributed in various organs of a heterogeneous phantom *MIRD Pamphlet No.5, revised, Society of Nuclear Medicine, New York N. Y.*

Walters B R B, Ding G X, Kramer R and Kawrakow I 2009 Skeletal dosimetry in cone beam computed tomography *Phys. Med.* ***36*** *(7) 2915-2922*

Xu X G, Chao T C, Bozkurt A 2000 VIP-MAN: An Image-based Whole-body Adult Male Model Constructed From Colour Photographs Of The Visible Human Project For Multi-particle Monte Carlo Calculations *Health Phys.* ***78****(5):476-486*

Xu X G, Taranenko V, Zhang J and Shi C 2007 A boundary-representation method for designing whole-body radiation dosimetry models: pregnant females at the end of three gestional periods – RPI-P3, -P6 and P9 *Phys. Med. Biol.* ***52*** *7023-7044*

Xu X G and Eckerman K F 2009 Handbook of anatomical models for radiation dosimetry, Edited by Xu G and Eckerman K, Taylor & Francis

Xu X G, Zhang J Y and Na Y H 2008 Preliminary Data for Mesh-Based Deformable Phantom Development: Is it Possible to Design Person-Specific Phantoms On-demand. The International Conference on Radiation Shielding-11, April 14-17

Zhang J Y, Na Y H and Xu XG 2008a Size Adjustable Worker Models For Improved Radiation Protection Dosimetry. Health Phys., Vol 95(1), S50

Zhang J Y, Na Y H and Xu X G 2008b Development of Whole-Body Phantoms Representing An Average Adult Male and Female Using Surface-Geometry Methods. Med. Phys., Vol 35(6), 2875

Zhang J, Na Y H, Caracappa P F and Xu X G 2009 RPI-AM and RPI-AF,a pair of mesh-based, size-adjustable adult male and female computational phantoms using ICRP-89 parameters and their calculations for organ doses from monoenergetic photon beams. Phys. Med. Biol. 54 5885-5908

Zankl M and Wittmann A 2001 The adult male voxel model "Golem" segmented from whole-body CT patient data *Radiat. Environ. Biophys.**40** 153-162*

Zankl M, Fill U, Petoussi-Henss N, Regulla D 2002 Organ dose conversion coefficients for external photon irradiation of male and female voxel models *Phys. Med. Biol. **47**, No.14, 2367-2386*

Zankl M, Eckerman K F and Bolch W E 2007 Voxel-based models representing the male and female ICRP reference adult—the skeleton *Rad. Prot. Dos. **127** 174-186*

APPENDIX

Table A1 shows the organs and tissues T to be taken into account for the calculation of the effective dose together with their tissue weighting factors according to ICRP103 (ICRP 2007). Effective doses for whole body AP and ROT incidence, calculated with the FASH and the MASH phantoms, are shown in table A2. In these calculations, equivalent doses H_T per air kerma K_a were determined in all organs and tissues T mentioned in table A1. For the urinary bladder, the colon, the small intestine, the stomach and the gall bladder, equivalent doses were determined for the walls. Tables A3 to A6 present CCs between equivalent doses H_T and air kerma K_a for the 14 organs and tissues of the main group with specific tissue weighting factors. Equivalent doses to all other organs and tissues are included in the remainder equivalent dose. The statistical errors were smaller than 1% for most organ and tissues equivalent doses for all photon energies and projections, with the following exceptions: 1.7% on average for bladder wall, oesophagus, salivary glands and testes; 2% on average for thyroid and male breasts (ROT) and 2.5% on average for ovaries.

Table A1. Weighting factors for organs and tissues T (ICRP 2007)

Bone marrow (red), Colon, Lung, Stomach, Breast, Remainder Tissues*	0.12
Gonads	0.08
Bladder, Oesophagus, Liver, Thyroid	0.04
Bone surface, Brain, Salivary glands, Skin	0.01

* Remainder tissues: Adrenals, Extrathorarcic region (ET), Gall bladder, Heart, Kidneys, Lymphatic nodes, Muscle, Oral mucosa, Pancreas, Prostate, Small Intestine, Spleen, Thymus, Uterus

Table A2. Effective dose E per air kerma K_a for external exposure to photons for AP and ROT incidence with 10 and 50 μm BSC layer thickness, calculated with the FASH and the MASH phantoms

Photon Energie (MeV)	AP_10 E/K_a (Sv/Gy)	AP_50 E/K_a (Sv/Gy)	ROT_10 E/K_a (Sv/Gy)	ROT_50 E/K_a (Sv/Gy)
0.01	0.008	0.008	0.004	0.004
0.015	0.048	0.048	0.021	0.021
0.02	0.128	0.128	0.058	0.058
0.03	0.404	0.403	0.201	0.200
0.04	0.757	0.753	0.417	0.414
0.05	1.064	1.057	0.628	0.623
0.06	1.260	1.251	0.778	0.772
0.07	1.361	1.352	0.871	0.863
0.08	1.362	1.353	0.890	0.883
0.1	1.322	1.315	0.888	0.883
0.15	1.188	1.184	0.827	0.825
0.2	1.124	1.121	0.796	0.794
0.3	1.047	1.046	0.765	0.764
0.5	0.997	0.996	0.767	0.766
1.0	0.979	0.978	0.795	0.795
3.0	0.970	0.969	0.858	0.858
6.0	0.926	0.926	0.846	0.845
10.0	0.857	0.855	0.819	0.820

FASH AP Energy (MeV)	RBM_10 H_T/K_a (Sv/Gy)	RBM_50 H_T/K_a (Sv/Gy)	Colon H_T/K_a (Sv/Gy)	Lung H_T/K_a (Sv/Gy)	Stomach H_T/K_a (Sv/Gy)	Breast H_T/K_a (Sv/Gy)	Remaind H_T/K_a (Sv/Gy)	Ovaries H_T/K_a (Sv/Gy)	Bladder H_T/K_a (Sv/Gy)	Oesoph H_T/K_a (Sv/Gy)	Liver H_T/K_a (Sv/Gy)	Thyroid H_T/K_a (Sv/Gy)	BSC_10 H_T/K_a (Sv/Gy)	BSC_50 H_T/K_a (Sv/Gy)	Brain H_T/K_a (Sv/Gy)	Saliv. H_T/K_a (Sv/Gy)	Skin H_T/K_a (Sv/Gy)
0.01	0.000	0.000	0.000	0.000	0.000	0.022	0.000	0.000	0.000	0.000	0.000	0.035	0.000	0.000	0.000	0.001	0.250
0.015	0.001	0.001	0.003	0.002	0.003	0.155	0.006	0.000	0.000	0.010	0.003	0.271	0.001	0.001	0.000	0.030	0.399
0.02	0.008	0.007	0.053	0.032	0.047	0.394	0.038	0.005	0.006	0.054	0.045	0.617	0.012	0.009	0.001	0.137	0.515
0.03	0.073	0.071	0.389	0.279	0.383	0.921	0.261	0.166	0.141	0.256	0.348	1.128	0.206	0.119	0.046	0.408	0.714
0.04	0.226	0.221	0.824	0.635	0.857	1.321	0.627	0.541	0.494	0.604	0.790	1.494	0.726	0.392	0.213	0.656	0.881
0.05	0.423	0.411	1.178	0.938	1.267	1.554	0.968	0.870	0.870	0.924	1.168	1.763	1.303	0.739	0.416	0.872	1.010
0.06	0.596	0.575	1.386	1.117	1.508	1.662	1.181	1.176	1.148	1.127	1.402	1.846	1.651	1.021	0.569	1.014	1.085
0.07	0.718	0.691	1.498	1.211	1.629	1.683	1.301	1.315	1.314	1.253	1.504	1.810	1.777	1.198	0.668	1.117	1.137
0.08	0.783	0.751	1.487	1.216	1.616	1.633	1.306	1.376	1.352	1.266	1.504	1.785	1.740	1.250	0.703	1.175	1.127
0.1	0.834	0.806	1.422	1.183	1.548	1.545	1.278	1.341	1.313	1.222	1.444	1.707	1.566	1.229	0.738	1.140	1.111
0.15	0.829	0.811	1.258	1.086	1.354	1.381	1.154	1.183	1.185	1.100	1.275	1.484	1.209	1.071	0.728	1.077	1.064
0.2	0.823	0.811	1.164	1.033	1.260	1.295	1.079	1.127	1.116	1.029	1.184	1.399	1.071	0.995	0.730	1.045	1.033
0.3	0.800	0.792	1.087	0.976	1.132	1.211	1.018	1.038	1.079	0.953	1.102	1.302	0.978	0.931	0.724	1.019	0.990
0.5	0.805	0.797	1.016	0.949	1.069	1.138	0.965	0.995	1.005	0.935	1.039	1.185	0.934	0.911	0.750	0.994	0.929
1.0	0.842	0.838	0.984	0.950	1.044	1.091	0.944	0.945	0.942	0.907	1.000	1.176	0.926	0.914	0.801	1.031	0.790
3.0	0.918	0.916	0.986	0.999	1.000	0.996	0.976	0.935	0.985	0.938	1.004	1.060	0.976	0.969	0.911	1.014	0.588
6.0	0.932	0.930	0.975	0.999	1.004	0.827	0.984	0.931	0.982	0.939	0.988	0.665	0.982	0.976	0.931	0.948	0.509
10.0	0.910	0.910	0.905	0.988	0.953	0.643	0.933	0.859	0.902	0.931	0.963	0.559	0.945	0.940	0.932	0.847	0.451

Table A3. Conversion coefficients between organ and tissue equivalent doses H_T and air kerma K_a for external exposure of the FASH phantom to photons for AP incidence with energies between 10 keV and 10 MeV. Equivalent doses to the red bone marrow (RBM) and the bone surface cells (BSC) are given for 10 and 50 μm BSC layer thicknesses.

FASH ROT Energy (MeV)	RBM_10 H_T/K_a (Sv/Gy)	RBM_50 H_T/K_a (Sv/Gy)	Colon H_T/K_a (Sv/Gy)	Lung H_T/K_a (Sv/Gy)	Stomach H_T/K_a (Sv/Gy)	Breast H_T/K_a (Sv/Gy)	Remaind H_T/K_a (Sv/Gy)	Ovaries H_T/K_a (Sv/Gy)	Bladder H_T/K_a (Sv/Gy)	Oesoph H_T/K_a (Sv/Gy)	Liver H_T/K_a (Sv/Gy)	Thyroid H_T/K_a (Sv/Gy)	BSC_10 H_T/K_a (Sv/Gy)	BSC_50 H_T/K_a (Sv/Gy)	Brain H_T/K_a (Sv/Gy)	Saliv. H_T/K_a (Sv/Gy)	Skin H_T/K_a (Sv/Gy)
0.01	0.000	0.000	0.000	0.000	0.000	0.009	0.000	0.000	0.000	0.000	0.000	0.010	0.000	0.000	0.000	0.008	0.209
0.015	0.000	0.000	0.002	0.001	0.001	0.068	0.003	0.000	0.000	0.002	0.002	0.098	0.000	0.000	0.000	0.075	0.337
0.02	0.006	0.006	0.023	0.018	0.015	0.181	0.019	0.001	0.002	0.013	0.019	0.248	0.010	0.007	0.002	0.184	0.431
0.03	0.071	0.071	0.178	0.178	0.155	0.456	0.143	0.047	0.055	0.116	0.167	0.570	0.182	0.103	0.088	0.396	0.593
0.04	0.222	0.221	0.422	0.436	0.410	0.694	0.381	0.199	0.214	0.343	0.427	0.861	0.644	0.344	0.326	0.595	0.736
0.05	0.404	0.398	0.655	0.670	0.667	0.854	0.624	0.415	0.422	0.578	0.677	1.050	1.139	0.643	0.568	0.782	0.848
0.06	0.565	0.553	0.811	0.818	0.829	0.929	0.788	0.581	0.603	0.768	0.852	1.181	1.445	0.892	0.738	0.909	0.915
0.07	0.681	0.661	0.904	0.907	0.937	0.969	0.892	0.693	0.704	0.876	0.951	1.245	1.561	1.053	0.836	0.978	0.955
0.08	0.733	0.711	0.916	0.921	0.971	0.952	0.904	0.736	0.733	0.891	0.957	1.275	1.526	1.097	0.865	0.995	0.954
0.1	0.779	0.761	0.900	0.910	0.931	0.921	0.900	0.775	0.737	0.880	0.943	1.215	1.355	1.074	0.878	1.007	0.945
0.15	0.776	0.765	0.811	0.849	0.852	0.854	0.833	0.705	0.702	0.830	0.855	1.091	1.063	0.937	0.846	0.951	0.907
0.2	0.766	0.758	0.780	0.821	0.819	0.831	0.800	0.643	0.651	0.789	0.814	1.033	0.948	0.880	0.828	0.927	0.888
0.3	0.747	0.744	0.747	0.796	0.771	0.816	0.760	0.623	0.630	0.753	0.784	0.986	0.859	0.824	0.812	0.914	0.853
0.5	0.752	0.751	0.739	0.794	0.766	0.813	0.770	0.634	0.640	0.773	0.774	0.969	0.828	0.808	0.814	0.896	0.815
1.0	0.783	0.782	0.770	0.813	0.773	0.837	0.797	0.676	0.658	0.827	0.792	0.985	0.833	0.825	0.840	0.921	0.714
3.0	0.866	0.865	0.829	0.897	0.874	0.855	0.868	0.725	0.777	0.872	0.861	0.972	0.902	0.896	0.900	0.929	0.556
6.0	0.886	0.886	0.857	0.930	0.894	0.805	0.861	0.747	0.808	0.899	0.879	0.851	0.910	0.903	0.911	0.833	0.497
10.0	0.875	0.876	0.848	0.905	0.852	0.719	0.848	0.721	0.837	0.871	0.853	0.716	0.886	0.882	0.900	0.755	0.454

Table A4. Conversion coefficients between organ and tissue equivalent doses H_T and air kerma K_a for external exposure of the FASH phantom to photons for ROT incidence with energies between 10 keV and 10 MeV. Equivalent doses to the red bone marrow (RBM) and the bone surface cells (BSC) are given for 10 and 50 μm BSC layer thicknesses.

MASH AP Energy (MeV)	RBM_10 H_T/K_a (Sv/Gy)	RBM_50 H_T/K_a (Sv/Gy)	Colon H_T/K_a (Sv/Gy)	Lung H_T/K_a (Sv/Gy)	Stomach H_T/K_a (Sv/Gy)	Breast H_T/K_a (Sv/Gy)	Remaind H_T/K_a (Sv/Gy)	Testes H_T/K_a (Sv/Gy)	Bladder H_T/K_a (Sv/Gy)	Oesoph H_T/K_a (Sv/Gy)	Liver H_T/K_a (Sv/Gy)	Thyroid H_T/K_a (Sv/Gy)	BSC_10 H_T/K_a (Sv/Gy)	BSC_50 H_T/K_a (Sv/Gy)	Brain H_T/K_a (Sv/Gy)	Saliv. H_T/K_a (Sv/Gy)	Skin H_T/K_a (Sv/Gy)
0.01	0.000	0.000	0.000	0.000	0.000	0.054	0.000	0.003	0.000	0.000	0.000	0.000	0.000	0.000	0.000	0.001	0.221
0.015	0.000	0.000	0.001	0.000	0.002	0.393	0.005	0.076	0.000	0.002	0.003	0.059	0.000	0.000	0.000	0.038	0.370
0.02	0.004	0.004	0.027	0.016	0.040	0.773	0.033	0.291	0.002	0.026	0.046	0.311	0.007	0.005	0.000	0.145	0.485
0.03	0.053	0.052	0.273	0.228	0.363	1.251	0.228	0.842	0.078	0.190	0.348	0.914	0.172	0.099	0.035	0.403	0.677
0.04	0.180	0.176	0.648	0.579	0.859	1.558	0.576	1.285	0.320	0.505	0.796	1.320	0.651	0.349	0.185	0.661	0.835
0.05	0.355	0.344	0.983	0.897	1.279	1.762	0.907	1.564	0.621	0.846	1.194	1.651	1.179	0.670	0.382	0.871	0.957
0.06	0.515	0.496	1.204	1.100	1.542	1.860	1.140	1.748	0.854	1.043	1.445	1.730	1.550	0.954	0.543	1.011	1.035
0.07	0.636	0.610	1.321	1.216	1.680	1.886	1.257	1.754	1.016	1.197	1.570	1.822	1.683	1.128	0.643	1.102	1.087
0.08	0.703	0.675	1.322	1.230	1.658	1.790	1.282	1.735	1.048	1.209	1.573	1.747	1.651	1.182	0.686	1.133	1.081
0.1	0.769	0.739	1.289	1.212	1.581	1.673	1.251	1.630	1.072	1.215	1.513	1.655	1.505	1.191	0.722	1.138	1.074
0.15	0.774	0.756	1.147	1.115	1.382	1.475	1.125	1.398	0.978	1.064	1.331	1.496	1.178	1.043	0.726	1.109	1.025
0.2	0.768	0.754	1.071	1.054	1.269	1.425	1.064	1.322	0.949	1.008	1.226	1.472	1.044	0.972	0.723	1.055	1.001
0.3	0.756	0.745	0.997	1.001	1.164	1.274	0.991	1.227	0.904	0.931	1.126	1.358	0.961	0.920	0.715	1.042	0.962
0.5	0.767	0.760	0.950	0.967	1.076	1.198	0.947	1.130	0.874	0.894	1.049	1.244	0.915	0.893	0.740	1.022	0.914
1.0	0.800	0.795	0.923	0.960	1.016	1.148	0.942	1.076	0.873	0.921	1.005	1.188	0.912	0.898	0.798	1.055	0.806
3.0	0.890	0.886	0.950	0.996	1.028	0.886	0.961	1.042	0.900	0.917	1.001	0.990	0.961	0.953	0.892	1.019	0.603
6.0	0.937	0.935	0.966	1.007	1.048	0.502	0.977	0.935	0.883	0.924	1.001	0.969	0.990	0.983	0.921	0.941	0.519
10.0	0.917	0.912	0.941	1.004	0.959	0.275	0.936	0.739	0.936	0.950	0.965	0.740	0.958	0.949	0.931	0.852	0.466

Table A5. Conversion coefficients between organ and tissue equivalent doses H_T and air kerma K_a for external exposure of the MASH phantom to photons for AP incidence with energies between 10 keV and 10 MeV. Equivalent doses to the red bone marrow (RBM) and the bone surface cells (BSC) are given for 10 and 50 μm BSC layer thicknesses.

MASH ROT Energy (MeV)	RBM_10 H_T/K_a (Sv/Gy)	RBM_50 H_T/K_a (Sv/Gy)	Colon H_T/K_a (Sv/Gy)	Lung H_T/K_a (Sv/Gy)	Stomach H_T/K_a (Sv/Gy)	Breast H_T/K_a (Sv/Gy)	Remaind H_T/K_a (Sv/Gy)	Testes H_T/K_a (Sv/Gy)	Bladder H_T/K_a (Sv/Gy)	Oesoph H_T/K_a (Sv/Gy)	Liver H_T/K_a (Sv/Gy)	Thyroid H_T/K_a (Sv/Gy)	BSC_10 H_T/K_a (Sv/Gy)	BSC_50 H_T/K_a (Sv/Gy)	Brain H_T/K_a (Sv/Gy)	Saliv. H_T/K_a (Sv/Gy)	Skin H_T/K_a (Sv/Gy)
0.01	0.000	0.000	0.000	0.000	0.000	0.014	0.000	0.003	0.000	0.000	0.000	0.000	0.000	0.000	0.000	0.008	0.193
0.015	0.000	0.000	0.001	0.000	0.000	0.133	0.003	0.051	0.000	0.000	0.001	0.020	0.000	0.000	0.000	0.072	0.329
0.02	0.003	0.003	0.012	0.006	0.012	0.295	0.017	0.167	0.001	0.006	0.015	0.119	0.006	0.005	0.001	0.176	0.427
0.03	0.051	0.050	0.126	0.109	0.132	0.560	0.122	0.459	0.035	0.080	0.138	0.434	0.151	0.085	0.065	0.377	0.588
0.04	0.176	0.175	0.340	0.325	0.365	0.738	0.336	0.702	0.169	0.269	0.367	0.753	0.562	0.300	0.284	0.574	0.724
0.05	0.343	0.337	0.561	0.551	0.595	0.864	0.557	0.862	0.363	0.503	0.606	1.006	1.038	0.591	0.536	0.752	0.832
0.06	0.494	0.481	0.734	0.712	0.776	0.935	0.734	0.976	0.504	0.702	0.776	1.130	1.348	0.833	0.710	0.874	0.901
0.07	0.611	0.593	0.828	0.813	0.872	1.002	0.832	1.009	0.632	0.787	0.870	1.190	1.476	0.990	0.823	0.967	0.946
0.08	0.671	0.651	0.853	0.839	0.881	0.968	0.863	1.022	0.668	0.823	0.901	1.226	1.447	1.042	0.856	1.008	0.944
0.1	0.728	0.707	0.847	0.841	0.891	0.926	0.864	1.021	0.699	0.837	0.890	1.203	1.325	1.045	0.879	0.997	0.941
0.15	0.747	0.734	0.789	0.793	0.807	0.880	0.810	0.930	0.683	0.772	0.814	1.062	1.055	0.932	0.849	0.959	0.909
0.2	0.732	0.725	0.749	0.764	0.767	0.866	0.770	0.875	0.646	0.736	0.771	1.033	0.948	0.867	0.825	0.947	0.889
0.3	0.716	0.712	0.718	0.747	0.730	0.807	0.746	0.837	0.633	0.715	0.735	1.010	0.849	0.814	0.816	0.911	0.858
0.5	0.725	0.723	0.719	0.747	0.728	0.831	0.747	0.876	0.646	0.719	0.729	0.962	0.823	0.802	0.819	0.905	0.824
1.0	0.764	0.764	0.746	0.782	0.758	0.887	0.771	0.874	0.707	0.752	0.754	0.967	0.831	0.819	0.844	0.902	0.741
3.0	0.854	0.853	0.818	0.862	0.831	0.834	0.836	0.870	0.755	0.815	0.841	1.012	0.895	0.889	0.914	0.900	0.570
6.0	0.888	0.889	0.854	0.902	0.836	0.679	0.854	0.801	0.830	0.855	0.854	0.891	0.918	0.911	0.923	0.833	0.504
10.0	0.884	0.883	0.842	0.898	0.842	0.597	0.852	0.719	0.836	0.901	0.846	0.802	0.898	0.893	0.906	0.742	0.458

Table A6. Conversion coefficients between organ and tissue equivalent doses H_T and air kerma K_a for external exposure of the MASH phantom to photons for ROT incidence with energies between 10 keV and 10 MeV. Equivalent doses to the red bone marrow (RBM) and the bone surface cells (BSC) are given for 10 and 50 μm BSC layer thicknesses.